Contact line dynamics near the pinning threshold: A capillary rise and fall experiment

Erik Schäffer* and Po-zen Wong

Department of Physics and Astronomy, University of Massachusetts, Amherst, Massachusetts 01003

(Received 13 September 1999)

We used video microscopy to study the pinning dynamics of air/water contact lines in vertical glass capillaries. Stick-slip behavior and avalanches are observed in tubes with rough interior walls and strong pinning forces. In tubes with smooth interior walls, we find that receding contact lines in falling water columns show no evidence of pinning, but advancing contact lines in rising water columns exhibit algebraic slow down. The measured value of the critical exponent β varies from run to run, but it is always larger than unity. Furthermore, we find that the rise dynamics varies with the waiting time preceding the experiments. These observations led us to conclude that the wetting film on the surface and other microscopic changes in the slipping region near the contact line affect the macroscopic dynamics. We discuss the differences between the real system and the existing theories that might explain the results. We also present a brief review of other studies of contact line dynamics and a numerical study of a one-dimensional model.

PACS number(s): 47.60.+i, 05.65.+b, 68.10.−m, 68.45.Gd

I. INTRODUCTION

The rise and fall of fluids in capillary tubes have been studied for many decades [1]. On the macroscopic scale, it is a simple experiment in a simple geometry. The equations for static and dynamic situations are well defined and widely used. On the microscopic scale, however, even in such a simple system, the imperfections of real surfaces and the presence of thin wetting films can have profound effects on the macroscopic dynamics. Since the flow of fluid through small pores and the spreading of liquids on solid surfaces have a wide range of applications in many fields of science and technology, there is much interest in understanding the connections between the microscale and macroscale behavior. The *contact line* of the vapor-liquid-solid phases is often the focal point of investigation. An interesting idea to describe the dynamics is in terms of a *depinning transition* and it has attracted considerable attention in recent years. A raindrop stuck on a windowpane offers the simplest illustration of this idea. The essence of it is that the geometric roughness and chemical disorder on the glass surface can be modeled by a random potential. It can pin the raindrop in a metastable state. If the weight of the drop exceeds the net pinning force, it would slide down, but it may be halted again if the air-water-glass contact line encounters stronger pinning forces. In this paper we report an experiment that uses the rise and fall of water columns in capillary tubes to study the dynamics near the depinning transition. Some of the highlights have been reported previously in Ref. [2] and some details not described here may be found in Ref. [3].

The effects of pinning and depinning, often described as stick-slip behavior, are seen in many different physical systems. Examples include the sliding of charge density waves in quasi-one-dimensional conductors with increasingly applied voltage [4], the motion of magnetic domain walls driven by an applied field [5,6], vortex flow in superconduct-

ing films [7], and the movement of fluid interfaces in porous media [8,9]. Common to all these systems is the presence of *quenched disorder*, or a random potential, that leads to pinning effects. The transition from the pinned state to a moving state has been proposed as an example of *dynamical critical phenomena* [10–12] that exhibit scaling behavior. Near the critical point, theories generally predict an algebraic form for the system's *average* velocity v,

$$v = v_o(F/F_c - 1)^\beta, \qquad (1)$$

where F is the driving force, F_c the finite pinning threshold, and β the critical exponent. β is believed to be universal [13–15] in the sense that it depends only on the dimensionality of the system and not on material details such as the nature of the order parameter, interactions, and disorder. For contact lines, the physical picture is that, superimposed on the overall velocity v, sections of the line make discrete ''jumps'' analogous to avalanches in other systems. The size of the jumps follows a power-law distribution and it is limited by a characteristic correlation length ξ. As in equilibrium critical phenomena, ξ diverges as

$$\xi \propto (F - F_c)^{-\nu} \qquad (2)$$

at the threshold F_c, where ν is the correlation length exponent. The roughness of the line is self-affine at length scales smaller than ξ. Its width w scales as

$$w \propto \xi^\alpha, \qquad (3)$$

where $\alpha = 1 - 1/\nu$ is the roughness exponent [15]. The average waiting time τ associated with a jump of size ξ obeys dynamic scaling with an exponent z:

$$\tau \propto \xi^z. \qquad (4)$$

These scaling relations predict an average velocity

$$v \propto \frac{w}{\tau} \propto \xi^{\alpha - z} \propto (F - F_c)^{-\nu(\alpha - z)} = (F - F_c)^\beta \qquad (5)$$

*Present address: LS Professor Dr. Mlynek, Fakultät für Physik, Universität Konstanz, Fach M695, 78457 Konstanz, Germany.

where the exponent $\beta = \nu(z-\alpha)$. Generally speaking, the data from various experimental systems seem to fit the algebraic form of Eq. (1) but the values of the exponent β differ considerably from the theoretical predictions. The cause of this discrepancy is not understood.

The capillary rise experiment we report here probes a wide range of velocities on surfaces with different roughness. We observed stick-slip behavior and evidence for scaling. However, the exponent β was irreproducible and indicated a dependence on the presence of a wetting film. The film properties appear to control the dynamics near the pinning threshold [2]. Similar microscopic details in other systems may also be responsible for the apparent lack of universality.

The paper is structured as follows. In Sec. II, we review the experimental and theoretical work on dynamic contact angles and contact line dynamics. Section III gives a mean-field description of the dynamics of capillary rise and fall in a vertical tube in the absence of surface disorder. This discussion defines the relevant variables in the experiment and the theoretical baseline for analyses. Section IV gives the experimental details and Sec. V presents the results for strong and weak surface disorder. In the strong disorder case, stick-slip behavior of the *entire* contact line was observed and attributed to finite-size effects. In that limit, the system becomes one dimensional (1D). As a result, we present a 1D simulation of the equation of motion in Sec. VI to compare with the data. In Sec. VII we summarize our findings and discuss several important differences between the real system and the theoretical models.

II. REVIEW OF BACKGROUND

Classically, Young's equation describes the *equilibrium* contact angle of a drop on an *ideal* flat surface. It can be modified to include a correction term for an adsorbed film, which must be present when the system is in equilibrium with its vapor-saturated atmosphere [16]. Wenzel [17] further modified Young's equation to include effects of a rough surface. Chemical heterogeneities were considered by Cassie [18]. Nonideal surfaces lead to *contact angle hysteresis*. Surface roughness and chemical heterogeneities, due to contamination or otherwise, introduce metastable states in the system. A receding or advancing contact line can become pinned when the contact angle falls in a range $\theta_r < \theta < \theta_a$ around the static equilibrium angle θ. The apparent contact angle measured while the liquid is retracting is called the *receding* angle, and that associated with liquid spreading is called the *advancing* angle. θ_r and θ_a correspond to the maximum receding angle and minimum advancing angle for a *moving* contact line. Their difference depends on the degree of roughness and heterogeneity. A further cause for hysteresis is the presence of solutes in the liquid. It can change the solid-liquid interfacial structure at the molecular level, and thereby the macroscopic surface tension.

In general, the apparent contact angle associated with a moving contact line varies with velocity. A number of empirical relationships and theoretical models for wetting have been discussed in the literature, all of which express the *dynamic* contact angle θ_d as a function of the capillary number Ca and the static advancing contact angle θ_a during spreading,

$$\theta_d = f(Ca, \theta_a). \tag{6}$$

The capillary number Ca is defined as the ratio of viscous and interfacial forces

$$Ca = \frac{\eta}{\gamma} v, \tag{7}$$

where v is the interface velocity, γ the surface tension, and η the viscosity of the liquid. For $Ca < 10^{-2}$, the most commonly suggested relationship is

$$\cos \theta_a - \cos \theta_d = A Ca^B \tag{8}$$

where A and B are constants. As shown in Eq. (14) below, this equation is equivalent to Eq. (5) if we identify $B = 1/\beta$. This result suggests that dynamic wetting has universal behavior that is independent of the details of the solid-liquid-gas system. While this is an interesting idea, a closer examination of the data in the literature reveals that this relationship was never observed over a wide range in Ca. We give a brief survey of the classical studies below first and then review the more recent theoretical and experimental results.

Elliot and Riddiford [19,20] studied the flow of water between glass and polyethylene plates. They found that the dynamic contact angle was constant to within 1% of the static advancing angle (approximately $100°$) for $Ca < 2 \times 10^{-7}$. Above that value, the angle increased monotonically until it reached a limiting plateau value of $115(1)°$ for $Ca < 2 \times 10^{-6}$. Schwartz and Tejeda [21] identified three regimes of wetting behavior in a study using ten different solid-liquid systems with static contact angles between $0°$ about $70°$ approximately. In the lowest range, $Ca < 2 \times 10^{-6}$, the dynamic contact angle is independent of velocity. This is followed by two regions where the contact angle becomes larger with increasing capillary number with a change of slopes at $Ca \approx 10^{-3}$. Blake [22] reports similar dynamic behavior. In addition, he observes the occurrence of stick-slip motion in the range of $10^{-5} < Ca < 10^{-3}$. Seebergh and Berg [23] reviewed and confirmed Eq. (8). They also tested the influence of intermolecular forces (acid-base interactions between the liquid and solid phases) on the dynamics of the contact angle for a variety of solids and liquids classified according to their chemical properties (acidic, basic, or neutral character). They concluded that the dynamic contact angle is unaffected by such interactions. Consequently, the wetting behavior in the presence of intermolecular forces (acid-base) cannot be differentiated from purely dispersive systems (acid-acid, base-base, or neutral with any other property). Both types of systems resulted in the same parameters A and B in Eq. (8).

The role of roughness in wetting has been investigated in several systems [21,22,24]. It has been established that roughness increases the dependence of the contact angle on the velocity of the interface and that it introduces stick-slip behavior in the low capillary number regime for systems with nonzero static contact angle. Cain et al. [24] reported velocity dependencies of the advancing dynamic contact

angle θ_d over a narrow range of Ca. They used silicone coated glass slides of various degrees of roughness and dipped them in water at rates of $0.8-12$ mm/s, which correspond to $10^{-8} < Ca < 10^{-7}$. For the smooth slides, an initial increase for small Ca in the contact angle is followed by a plateau region and another increasing region. The plateau section and the onset of the second rise coincide with the data from Elliot and Riddiford. However, the initial increase of the contact angle for very low velocities was not reported before. Using slides with rough surfaces, they found that the plateau region disappeared. They attributed the initial rise with increasing Ca to a diffusive mechanism and *not* a viscous (velocity) effect. They argued that if the dipping of the slide was slow enough, a thin film ahead of the contact line on the initially dry surface would be established by the adsorption of the diffusing vapor and this could affect the contact angle. If the dipping velocity is faster than the establishment of the adsorbed film, the surface properties would remain unaltered. Thus the contact angle would be insensitive to the velocity in the low Ca limit. Their results demonstrate the importance of making measurements in a vapor-saturated atmosphere in thermal equilibrium.

Elliot and Riddiford [20], as well as Hansen and Miotto [25] before them, suggested a *kinetic* interpretation for the constant contact angle at low capillary numbers ($Ca < 10^{-7}$). In their scaling approach, they compare the interfacial velocity v with a natural displacement velocity v_n defined by the ratio of a characteristic film thickness L_{film} near the contact and the relaxation time τ_{mol} of the slowest molecules in the periphery. If $v < v_n$ the molecules in the liquid have enough time to find their equilibrium positions with respect to the solid surface, and the contact angle should be independent of the velocity. L_{film} is expected to be of molecular size, and τ_{mol} varies with the materials used. For the water-silicone system studied, the transition from the static to the dynamic contact angle was found to occur at velocities that correspond to $Ca \approx 10^{-7}$, which resulted in the estimate $\tau < 10^{-5}$ s. The difference from the relaxation time $\tau_0 \approx 10^{-10}$ s for bulk water is attributed to the energy barrier for adsorbing liquid molecules onto the surface. The disagreement with the study of Cain *et al.* may be explained by the lack of vapor pressure control in the latter experiment. So the real effects of surface roughness and heterogeneities remain unclear.

A. The depinning transition

As we have mentioned, the recent ideas about the effects of surface disorder center around the notions of avalanches and dynamical phase transitions. The same set of ideas and phenomenology apply to fluid interfaces moving through a random porous media as well. Koplik and Levine [10] suggested a stochastic differential equation to describe the dynamics of fluid interfaces in porous media with quenched disorder. Their model assumes that the interface is nearly flat so that they can ignore the possibility of overhangs and pinched off patches of the displaced fluid. The position of the interface is represented by a single valued function $z = f(\mathbf{x}, t)$, $\mathbf{x}$ being a $(d-1)$-dimensional transverse vector. In $(1+1)$ dimensions, $(1$ transverse + 1 parallel direction with respect to the driving force), z may be thought of as the
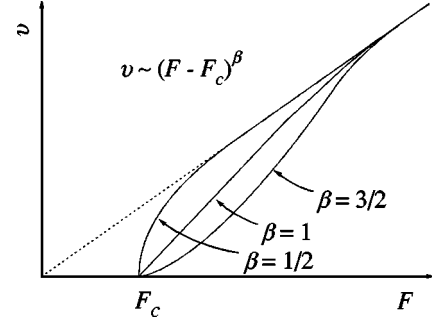

FIG. 1. Depending on whether the exponent β is greater than, equal to, or smaller than unity, the velocity goes to zero at the critical point F_c with zero, finite, or infinite slope, respectively.

position of a contact line. In $(2+1)$ dimensions, z may be used to describe a fluid interface in porous media. The equation of motion is argued to be

$$\frac{\partial f}{\partial t} = v_\infty + J\nabla^2 f + Y(\mathbf{x}, f), \tag{9}$$

where v_∞ is the macroscopic interface velocity that would result from a uniform driving force F in the absence of the other terms on the right-hand side. In the case of fluid flow in porous media, for example, v_∞ is proportional to the applied pressure gradient (Darcy's law). The ∇^2 term in Eq. (9) represents a spatially varying capillary force due to the local curvature of the interface. It can be interpreted as an effective surface tension that acts to minimize the interfacial area or interfacial free energy. J is an effective elasticity. $Y(\mathbf{x}, f)$ represents the quenched disorder in the system. For short-range uncorrelated disorder, Y should be δ correlated and have zero mean.

Equation (9) has been analyzed by Nattermann *et al.* [12], and independently by Narayan and Fisher [13], using functional renormalization-group (RG) methods. From an ϵ expansion around five dimensions ($d = 5 - \epsilon$), they obtained essentially the same behavior for the *depinning transition* as summarized in Eqs. (1)-(5). Figure 1 illustrates the key feature of the transition: the velocity approaches zero at a finite threshold force F_c according to Eq. (1). Three cases of different exponent ($\beta > 1$, $\beta = 1$, and $\beta < 1$) are depicted and they have different asymptotic slopes at the critical point (zero, a finite constant, and infinity).

B. Theoretical predictions

The RG analysis of Eq. (9) with $\epsilon = 5 - d$ predicts [12,13]

$$\alpha = 2 - 1/\nu = \epsilon/3 \tag{10}$$

and

$$\beta = (z - \alpha)\nu = 1 - \epsilon/9 + O(\epsilon^2). \tag{11}$$

Since contact lines may be regarded as belonging to the $(1+1)$-dimension universality class, which corresponds to $d = 2$ and $\epsilon = 3$, we obtain $\alpha = 1$ and $\beta \approx 2/3$. However, Ertaş and Kardar [15] noted that the free energy associated with the contact line is different because it involves three different phases while Eq. (9) is intended for two-phase systems. The

TABLE I. Theoretical predictions and studies for the critical exponent β.

Reference		Ca	β
Tanner (1979) [40]	complete wetting, precursor, smooth surface	small	3/2
Hoffman (1983) [30]	diffusion mechanism, smooth surface	$10^{-5}-10^{-3}$	1
Cox (1986) [35]	slipping models, smooth surface	small	1
Mumley et al. (1986) [46]	dissipation in film, prewetted smooth surface	$10^{-4}-10^{-2}$	≈ 2
		$<10^{-5}$	1
Ishimi et al. (1986) [37]	complete wetting, precursor, rough surface	small	2
Raphaël and de Gennes (1989) [38]	smooth surface, partial wetting;	small	1
	chemical mono defects: constant force		1/2
	constant velocity		3/2
Joany and Robbins (1990) [39]	partial wetting, periodic defects	small	
	constant force: heterogeneity		
	sine wave		1/2
	square wave		1
	triangular wave		$\bar{v} \propto \ln(F/F_c-1)$
	constant velocity: weak pinning		1
	strong pinning		3/2
Sheng and Zhou (1992) [31]	smooth surface	$10^{-3}-10^{-2}$	1
	rough surface, capillary wave excitation	$<10^{-3}$	$2-\infty$
Nattermann et al. (1992) [12]	renormalization group (RG) in		
	$d=5-\epsilon$ dimensions (interfaces)		2/3
Narayan and Fisher (1993) [14]	RG in $d=5-\epsilon$ dimensions (interfaces)		2/3
Ertaş and Kardar (1994) [15]	RG in $D=2-\epsilon$ interface dimensions (contact lines)		2/3

fluctuations of the contact line not only affect the liquid-solid and vapor-solid interfaces, but they also deform the liquid-vapor interface [26]. Using an ϵ expansion for interface dimensions D near 2 ($\epsilon=2-D$), they predict

$$\alpha = \epsilon/3 \qquad (12)$$

and

$$z=1-2\epsilon/9+O(\epsilon^2). \qquad (13)$$

Contact lines correspond to $D=1$, and hence $\alpha=1/3$, and $z \approx 7/9$. The scaling laws $\beta=\nu(z-\alpha)$ and $\nu=1/(1-\alpha)$ give $\beta \approx 2/3$ and $\nu=3/2$, respectively.

In addition to the RG analyses, a number of mean-field theories have been developed for the moving contact line and they generally obtained Eq. (8) as their prediction for the dynamic contact angles. The exponent B may be related to the scaling exponent β in Eq. (1) by the following consideration. We note that the excess force acting on the advancing contact line can be expressed in terms of the dynamic and static angles

$$F-F_c \propto \gamma(\cos\theta_a-\cos\theta_d) \propto ACa^B \propto v^B. \qquad (14)$$

A direct comparison to Eq. (1) leads to the identification

$$\beta=1/B. \qquad (15)$$

Thus an experiment that measures the dynamic contact angle as a function of the capillary number Ca can be used to determine the scaling exponent β.

The difficulty in using hydrodynamic models to calculate the dynamic contact angle has to do with the well-known nonintegrable singularity in the stress at the contact line. It results in a divergence in the energy dissipation [27]. To avoid this problem, the standard no-slip boundary condition has to be relaxed. The exact process of how the contact line moves is not totally understood at the molecular level. If the fluid wets the solid completely, one solution is to take into account the presence of a precursor film on which the bulk fluid spreads, so there is no true contact line. In the case of partial wetting, a rolling [28,29] or tank tread [30] motion like a tire rolling over a surface without slipping has been suggested.

On the mesoscopic scale, a number of slipping models have been proposed [31]. They all involve a characteristic slipping length l_s, a distance near the contact line over which continuum hydrodynamics break down. Molecular-dynamics simulations for a smooth surface suggest that $l_s \approx 10$ Å [32,33]. Clearly, for a rough surface, it is important to consider whether the contact line follows the contours of the surface continuously or jumps between metastable configurations. In all theoretical treatments of the dynamic contact angle, the microscopic details of the models proved to affect the macroscopic predictions. In other words, there was no universality. The following is a review of the various approaches and a summary is given in Table I.

Hoffman [30] assumed a microscopic picture in which the liquid molecules advance by a surface diffusion mechanism on a periodic lattice of the solid. His model is justified by field-ion microscopy data which show that ordered layers are formed in the adsorbed film due to the solid substrate potential [34]. This results in a tank tread motion for contact angles larger than $120°$. The equation he obtained corresponds to $\beta=1$ over the range of roughly $10^{-5}<Ca <10^{-3}$.

A hydrodynamic approach by Cox [35] uses a general slipping model and a matched asymptotic expansion involving the dynamic contact angle. He assumes a smooth surface and also obtains $\beta=1$ for $Ca\ll1$. This is attributed to the governing viscous forces near the contact line at low capillary numbers. In addition to the usual slipping models, non-Newtonian effects due to gradients in the surface tension or the elasticity of the solid may relieve the singularity at the contact line.

A treatment of the contact line motion in the presence of an adsorbed film is given by Mumley *et al.* [36] in the context of prewetted capillaries. The main assumption, following from lubrication theory, is that the energy dissipation takes place mainly within the film due to higher velocity gradients ∇v. If the film thickness b_0 (of the order of 1 μm) is much smaller than the tube radius R, than $\nabla v_{film}\propto1/b_0$ inside the film and $\nabla v_{bulk}\propto1/R$ in the bulk fluid. With this approximation, no dissipation takes place in the bulk and the adsorbed layer shields any surface roughness. Mumley *et al.* [36] obtained $\beta\approx2$ for $10^{-4}<Ca<10^{-2}$ and $\beta\approx1$ for $Ca<10^{-5}$. In the experiments performed, stick-slip behavior and jumps were observed even though a prewetting film was present. When the contribution of the jumps to the energy dissipation was included, they found that only the magnitude of the contact angle response changed, but not the exponent. Overall, it resulted in a better fit of their data.

Ishimi *et al.* [37] considered the situation of complete wetting in the presence of a precursor film. The idea is that the energy dissipation is caused by a frictional force acting on the film due to motion over a rough surface. This force is balanced by the interfacial tension on the precursor. The analysis led to $\beta=2$.

For the partial wetting case, Raphaël and de Gennes [38] considered a moving contact line being pinned only by one defect at a time. The macroscopic dynamics for the contact line were obtained by performing a time-average of the effect. For a flat homogenous surface without any defect, they obtained $\beta=1$. This results from intrinsic deformation of the contact angle at small capillary numbers due to hydrodynamic dissipations, which was also found by Hoffman and Cox. As in other calculations, the slipping length l_s appears in their equations. For a flat surface with smooth chemical heterogeneities that are spatially well separated, Raphaël and de Gennes considered two separate physical scenarios: imposing a constant velocity on the contact line or applying a constant force. For fluids in a capillary tube, these scenarios could be realized by pushing the liquid with a syringe pump at constant flow rate or letting the fluid column evolve under the influence of gravity. For the case of constant velocity, the pinning forces are averaged over time and this gives $\beta=3/2$. In the constant force case, the velocity fluctuations are averaged and it results in $\beta=1/2$. The analysis is only valid for single, smoothly varying defects—one at a time. For defects with sharp edges, called *mesa* defects, surface roughness probably results in different behavior.

Joanny and Robbins [39] studied similar scenarios for various periodic defects on solid surfaces. For the case of complete wetting, where a precursor is present and the contact line rides on top of the film, they obtained Tanner's law [40,26] behavior: $\theta_d\propto Ca^{1/3}$ when $Ca\ll1$. Since the static advancing angle $\theta_a=0$ for complete wetting, the functional

form of Eq. (8) can be obtained by using the Taylor series expansion for the cosine ($\cos x\approx1-\frac{1}{2}x^2$, for $x\ll1$), which gives $B=2/3$. According to Eq. (15), this corresponds to $\beta=3/2$. Using one of the slipping models, they obtained different results depending on the strength and the form of the defects and whether the force or the velocity is held constant. (The lubrication approximation again enters in form of a slipping length l_s.) The heterogeneities considered were assumed to be caused by chemical contaminations and consisted of periodic stripes. The strength of the individual defects had different functional forms. For constant applied force, the analysis gave $\beta=1/2$ for periodic stripes with a sine wave cross section, $\beta=1$ for a square wave, and a logarithmic dependence ($\beta=0$) for a triangular wave. In the constant velocity analysis, they obtained $\beta=1$ for weak pinning and $\beta=3/2$ for strong pinning. Strong pinning is characterized by having metastable positions where the contact line is pinned and the critical regime in which the power-law behavior can be observed is very small. Weak pinning only causes continuous deformations of the line. The difference between the two scenarios can be understood in simple physical terms: If a constant force is imposed, the power-law results from the fluctuations in the velocity of the contact line, which spends more time on the less wettable regions. In the constant velocity case, the fluctuations in the force in moving through different regions are weighted equally. In other words, letting either v or F be the fluctuating variable in Eq. (1) affects the statistical average over time. The values of the exponent β obtained by Joanny and Robbins are believed to be artifacts due to the assumed periodic geometries. In real systems, jumps or avalanches occur for portions of the contact line. Excited capillary waves change the coupling between the line and the defects. These may all change the results.

A different approach is taken by Sheng and Zhou [31]. They also assumed a slipping model and confirmed that viscous effects would give an intrinsic $\beta=1$ behavior for small capillary numbers, but they proposed a capillary-wave dissipation mechanism for $Ca<10^{-3}$ that modified the result. In their picture, a contact line moving across a rough surface performs nearly periodic jumps with a frequency that depends on the mean spacing between defects and the velocity of the line. The periodic motion excites capillary waves propagating along the interface and this is believed to be the dominant dissipation mechanism for $Ca<10^{-3}$. The analysis results in $2<\beta<\infty$, depending on the smoothness of the heterogeneities. Mesa defects give $\beta=2$.

C. Experimental results

Similar to the theoretical models, experimental studies using different techniques in different systems have found a wide range of values for the pinning exponent β over different ranges of Ca. The results show that the microscopic details near the contact line are important. We briefly review the most relevant literature below in chronological order. A summary is given in Table II.

Schwartz and Tejeda [21] measured the dynamic contact angle by dipping filaments with various degrees of roughness into several liquids. The data suggest $1\le\beta\le3$ for capillary numbers in the range $10^{-5}<Ca<1$. The degree of rough-

TABLE II. Experimental results for the critical exponent β.

Reference	Experiment	Ca	β
	Dynamic contact angle measurements		
Schwartz and Tejeda (1972) [21]	dipping cylindrical filaments (plastic, metal) with various degrees of roughness into several liquids (organic liquids, water)	$10^{-5}-1$	$1-3$
Jiang et al. (1979) [41]	liquid-air interfaces in capillaries (silicone fluids)	$<10^{-2}$	≈ 1.4
Rillaerts and Joos (1980) [43]	organic liquids (parafin oils, aqueous glycerol solutions) in prewetted capillaries	$4\times10^{-4}-4\times10^{-2}$	≈ 2
Ishimi et al. (1986) [37]	polyester tapes immersed into various liquids (water, different oils, and alcohols)	$10^{-6}-10^{-2}$	2
Mumley et al. (1986) [36,46]	capillary rise for liquid/liquid systems (glycerol–water solutions/ several hydrocarbons and silicones)	$10^{-5}-10^{-2}$	≈ 2
Bracke et al. (1989) [47]	plastic tape immersed into several liquids (corn oil, aqueous glycerin, ethylene-glycol solutions)	$3\times10^{-3}-10^{-1}$	≈ 2
Ström et al. (1990) [48]	dipping plate method using various solid/liquid systems (polystyrene, polytetrafluoroethylene/silcone oils, polyethylene glycols, paraffin oil, glycerol)	$10^{-7}-10^{-4}$	$\approx 3/2$
	ac method using the pressure response of liquid/liquid interfaces in capillaries		
Stokes et al. (1990) [49]	glycerol-methanol mixtures/mineral oils	$5\times10^{-5}-5\times10^{-4}$	2.5(4)
Kumar et al. (1995) [52]	water/alcanes	$10^{-6}-10^{-4}$	5(1)

ness did not seem to affect the exponent. Jiang et al. [41] analyzed the data obtained by Hoffman [42] who measured dynamic contact angles of liquid-air interfaces in capillary tubes. They found $\beta\approx1.4$ for $3\times10^{-5}<Ca<10^{-2}$. Rillaerts and Joos [43] used several organic liquids to determine the dynamic contact angle in prewetted capillaries and they found that $\beta\approx2$ for $4\times10^{-4}<Ca<4\times10^{-2}$.

To test their theoretical predictions, Ishimi et al. [37] analyzed data obtained by Kennedy and Burley [44] and those by Guthoff and Kendrick [45]. The experiments involved dipping polyester tapes into various liquids (water, different oils, and alcohols) and measuring the dynamic contact angle. Over a range of $10^{-6}<Ca<10^{-2}$, the data fit $\beta=2$ with an average deviation of 3.8% for the contact angle.

Mumley et al. [36,46] studied capillary rise of a polar liquid (glycerol-water solution) displacing a nonpolar liquid (several hydrocarbons and silicones). The tubes were prewetted with the wetting fluid and then either used directly with a wetting film present or dried before the experiment. For $10^{-5}<Ca<10^{-2}$ their data are consistent with $\beta\approx2$. Bracke et al. [47] made dynamic contact angle measurements using plastic tapes (e.g., polyethylene) immersed in several liquids (corn oil, aqueous glycerin, and ethylene-glycol solutions). They also found $\beta\approx2$ for velocities corresponding to $3\times10^{-3}<Ca<10^{-1}$.

Using a dipping plate method for various solid-liquid systems, Ström et al. [48] obtained $\beta\approx3/2$ for $10^{-7}<Ca<10^{-4}$. The liquids studied included silicone oils, polyethylene glycols, paraffin oil, and glycerol. The solids used included polystyrene and polytetrafluoroethylene. Their results agree with the small Ca limit of Tanner's law for complete wetting, but only some of the their systems were completely wetting such that a precursor film was present. The data from the partially wetting systems fitted equally well to the same exponent.

In more recent years, Stokes et al. [49] used a different technique [50,51] to determine the exponent β for a liquid-liquid meniscus in a capillary tube. They applied an ac velocity perturbation on top of a uniform dc velocity and measured the nonlinear pressure response. The meniscus has two possible modes of oscillation: it can slide back and forth as a whole and it can flex like a vibrating membrane. Due to mass conservation, the two modes are coupled. By keeping the modulation frequency below a threshold (of the order of 1 Hz), the flexing motion was suppressed and the contact line slides rigidly on the surface. The ac amplitude was small compared to the dc velocity to ensure that the meniscus always moves in the forward direction. The instantaneous velocity variation causes changes in the dynamic contact angle and the driving pressure, which correspond to θ_d and F in Eq. (14). For low capillary numbers Ca, the viscous pressure drop can be ignored and the ac pressure response may be regarded as due entirely to changes in the contact angle. Thus by detecting the pressure oscillation and analyzing its harmonics with Eq. (14), the exponent B (or $1/\beta$) can be determined [31]. Stokes et al. used a glycerol-methanol mixture as the more wetting fluid to displace a mineral oil. For $5\times10^{-5}<Ca<5\times10^{-4}$ they found $\beta\approx2.5(4)$. In a subsequent experiment using the same ac method, Kumar et al. [52] obtained $\beta\approx5(1)$ for water-alkane interfaces over the range $10^{-6}<Ca<10^{-4}$. We note that because these experiments measure B, a small absolute error ΔB can result in a large absolute error for β, though the relative errors $\Delta B/B$ and $\Delta\beta/\beta$ are the same. The large differences in β between these experiments may be attributed to the fact that one used a mixture while the other used a pure liquid. The viscosity of these liquids and their interactions with the solid surfaces are also different.
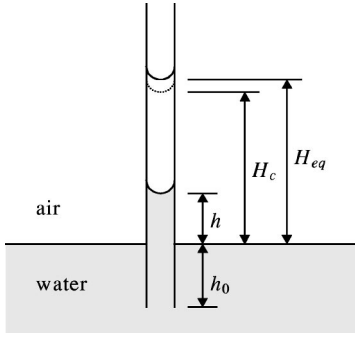
FIG. 2. Different height variables are shown in this illustration of a capillary rise experiment. H_c is the same as $H_c r$ in Sec. III B.

III. CAPILLARY RISE AND FALL

A. Washburn (mean-field) dynamics

In our study we chose to use capillary rise and fall to measure the exponent β because a wide range of capillary number Ca could be achieved. We were able to measure velocities in the range of $10^{-2} < v < 10^4$ μm/s, which corresponds to $10^{-10} < Ca < 10^{-4}$, a range that is both wider and lower than any previous study. To keep the chemistry less complicated we used deionized water and cleaned glass tubes in a vertical setup. A main assumption in our analysis is that the contact angle in our system is constant for $Ca < 10^{-7}$. For $10^{-7} < Ca < 10^{-4}$ where other studies have found varying dynamic contact angles, we did not find any evidence that it affected the macroscopic dynamics. Our experiment is somewhat similar to the controlled-force method described by Raphaël and de Gennes [38] and Joanny and Robbins [39], except that the force is not held constant. The system evolves under gravity and therefore approaches the pinning threshold in a self-organized manner. In this way all extraneous effects introduced by an external driving device (e.g., a mechanical pump) at low capillary numbers are eliminated. By performing both capillary rise and fall experiments, we are able to estimate the size of the defect strength and the pinning region. In addition, we can test if the critical behavior is different for the advancing and receding contact line.The presence of a wetting film is expected to play different roles in the two cases. In order to understand the pinning region, however, it is necessary to first understand the mean-field behavior in the absence of disorder.

Historically, Washburn [1] was the first to analyze the flow of liquid inside a capillary tube driven by a constant capillary pressure (contact angle). Figure 2 defines the variables in a capillary rise experiment. The equation of motion is obtained by equating the viscous damping force to the net driving force due to surface tension and gravity,

$$8\pi\eta(h+h_0)\frac{dh}{dt} = 2\pi r\gamma\cos\theta - \pi r^2\rho g h. \tag{16}$$

Here h is the height of the liquid column above the reservoir, h_0 is the length of capillary tube immersed in the liquid, r is the radius of the tube, and ρ is the density of the liquid. Inertial forces can be ignored in the overdamped limit where the tube radius is below a critical value r_c. It has been shown that [53]

$$r_c = \left(\frac{32\eta^2\gamma\cos\theta}{\rho^3 g^2} \right)^{1/5}. \tag{17}$$

For our system with water and air at room temperature, this expression gives $r_c \approx 0.4$ mm. Departure from the Poiseuille flow near the inlet and the meniscus are ignored in Eq. (16). It predicts an exponential approach to the equilibrium height

$$H_{eq} = 2\gamma\cos\theta/\rho g r \tag{18}$$

with a time constant

$$\tau_w = 8(h_0 + H_{eq})\eta/\rho g r^2. \tag{19}$$

We observe that $H_{eq} \propto r^{-1}$ and $\tau_w \propto (h_0 + H_{eq})/r^2$. So for tubes with smaller radii, the columns would rise higher and would take more time to reach H_{eq}. Using a normalized time variable $x \equiv t/\tau_w$ and a normalized height variable $y \equiv (h + h_0)/(H_{eq} + h_0)$, Eq. (16) can be expressed as

$$y\frac{dy}{dx} = (1 - y). \tag{20}$$

Integrating with initial height $h = h_i$ at time $t = 0$ yields the full solution known as the Washburn equation:

$$x - x_o = -y - \ln(1 - y), \tag{21}$$

where $x_o = -y_i - \ln(1 - y_i)$ and $y_i = (h_i + h_0)/(H_{eq} + h_0)$.

B. Critical dynamics of pinning

As the water meniscus approaches the equilibrium height, the driving force on the right-hand side of Eq. (16) diminishes and the random pinning forces become increasingly important. We expect the initial rise to obey the Washburn dynamics, followed by a crossover region, and finally enter a critical pinning region as the velocity tends to zero. For capillary rise, the meniscus would stop at a height H_{cr} below the equilibrium height H_{eq} (see Fig. 2), but for capillary fall, the meniscus would be pinned at a height H_{cf} above H_{eq}. The difference $(H_{cf} - H_{cr})$ gives an estimate for the size of the critical region. We found that the onset of critical behavior roughly corresponded to capillary numbers $Ca < 10^{-7}$ in our experiment. It is reasonable to assume that the average contact angle is *independent* of the velocity in this range. Microscopically, the contact line is distorted and so the local contact angle must vary with position. The apparent static advancing (receding) angle for capillary rise (fall) is observed on a macrospic scale when the meniscus comes to a stop and it should correspond to some kind of *average* value.

The critical pinning force for capillary rise is given by

$$F_c = \pi r^2\rho g(H_{eq} - H_c) \equiv \pi r^2\rho g H_{gap}, \tag{22}$$

where we have used H_c to denote H_{cr}. For low Ca, we can ignore the viscous force and the net driving force is given by

$$F = \pi r^2\rho g(H_{eq} - h). \tag{23}$$

Substituting F and F_c into Eq. (1) gives the equation of motion near the pinning threshold:
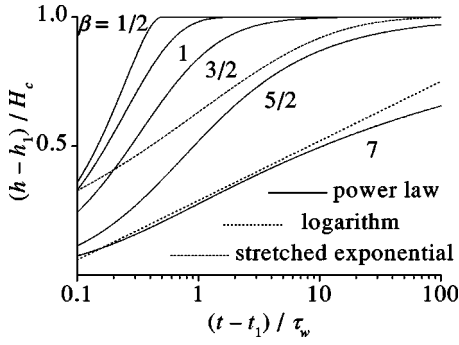
FIG. 3. The value of the exponent can cause qualitatively different behavior in how the water column height h approaches the pinned position H_c. Following Eq. (24), there are three scenarios: (i) for $\beta < 1$, the meniscus is pinned at a finite time $t = t_1 - 1/A$ (with $A < 0$); (ii) for $\beta = 1$, h approaches H_c exponentially, and (iii) for $\beta > 1$, h approaches H_c algebraically. Case (iii) may resemble a logarithmic or stretched exponential function if β is significantly larger than unity.

$$v = \frac{dh}{dt} = v_o \left(\frac{H_c - h}{H_{gap}} \right)^{\beta}. \tag{24}$$

For $\beta \neq 1$, integrating Eq. (24) from initial time t_1 and height h_1 yields

$$h(t) = H_c - (H_c - h_1)[1 + A(t - t_1)]^{1/(1-\beta)}, \tag{25}$$

where $A = (\beta - 1)v_o(H_c - h_1)^{\beta - 1}/H_{gap}^{\beta}$. This solution has the feature that if $\beta < 1$, h stops at H_c after a finite time $(t - t_1) = -1/A$. If $\beta > 1$, h approaches H_c algebraically as $t \to \infty$. In the special case of $\beta = 1$, the integration of Eq. (24) results in an exponential approach to H_c

$$h(t) = H_c - (H_c - h_1)e^{-(t-t_1)/\tau_1}, \tag{26}$$

where $\tau_1 = H_{gap}/v_o$. Figure 3 illustrates the qualitatively different behavior of Eq. (25) for different values of β. We note that the dynamics are the fastest for $\beta < 1$: the contact line reaches H_c after finite time. For large values of β, the dynamics are very slow and may not be easily distinguished from a logarithmic function. Other empirical functions such as a stretched exponential or an algebraic approach can also show similarly slow behavior. Fitting data to these different functions enables us to assess the reliability of the fitting parameters we obtained and the overall meaning of the interpretation. Since both capillary rise and fall can be performed in the same tube and our data in Sec. IV show that $H_{eq} \approx H_{cf}$, we can take $(H_{cf} - H_{cr})$ to be the same as H_{gap}. This is a useful indicator of the pinning strength F_c. It can also be used as an estimate of the size of the critical region. Having these estimates reduces some uncertainties in the data analyses.

IV. EXPERIMENTAL DETAILS

A. Samples

The capillary tubes that we studied have inner diameters (ID) ranging from 180 to 400 μm. Two types of tubes with different interior wall roughness were used. We shall refer to
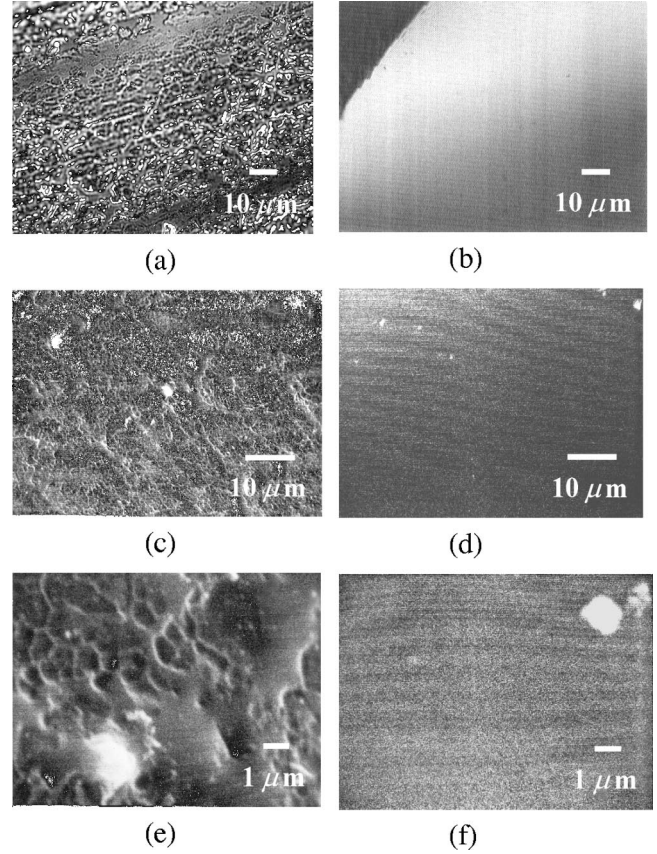

FIG. 4. The interior wall roughness of type R and type S capillaries can be seen with an optical microscope [(a) and (b)] and a SEM [(c)–(f)] using a wide range of magnifications. The R tubes [(a), (c), and (e)] clearly have a much higher level of roughness compared to the S tubes [(b), (d), and (f)]. The white spots on the SEM pictures are small glass particles left on the surface for marking position.

these as type R and S, for rough and smooth walls, respectively. Under both optical and scanning electron (SEM) microscopes, the S tubes show no evidence of roughness down to a nanometer resolution. Figure 4 shows SEM pictures at different magnifications and the difference in roughness between the two types of tube wall is evident at every scale.

The R tubes we used have ID's of 250, 310, and 410 μm. The S tube ID's were 180, 200, 250, 300, and 355 μm. The outside diameter for both types was about 0.5 mm and the length was about 30 mm. Both the R and the S tubes were made of borosilicate, low expansion, type-I glass (Corning Code 7740). The R tubes were obtained from ACE Glass Inc. and the S tubes from Friedrich & Dimmock. To clean and prepare the tubes for the experiment, we flow 400 ml of 1 M hydrochloric acid through it in about an hour. This was followed by approximately the same amount of deionized water at the same rate for rinsing. Finally, the capillaries were boiled in deionized water for about 8 h. By this process, the glass surface was well hydrated and reproducible results were obtained, though we probably did not remove all contaminants. In particular, because no organic solvents were used, some organic contaminants might be present. Immediately after the cleaning procedures, the capillaries were placed in the experimental apparatus.

(a)

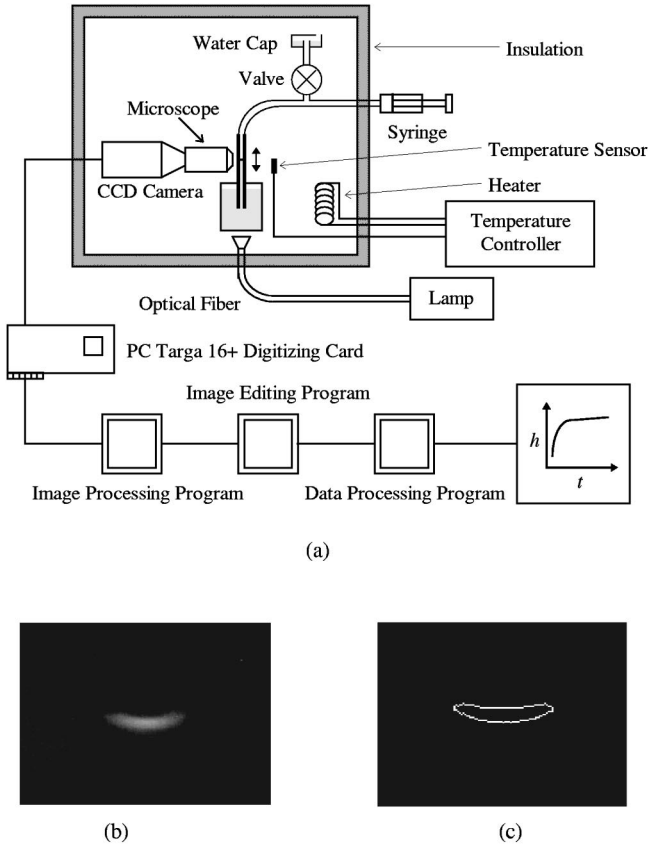(b)   (c)

FIG. 5. (a) An illustration of the experimental setup and data acquisition system. (b) A typical gray-scale image of an illuminated meniscus seen with the video microscopy system. (c) Binary bitmap image of the edge of the meniscus in (b), obtained by a simple edge detection algorithm.

B. Apparatus

Figure 5(a) shows a schematic drawing of the setup. The capillary stands vertically in a beaker containing deionized water. Attached to the top of the capillary is a Teflon tubing that connects it to a syringe that is used to raise or lower the water column to its initial height. A valve connects the tubing to a small cup half-filled with water which has a small hole on the cover plate. The purpose of the cup is to provide a 100% relative humidity atmosphere at ambient pressure. When the valve was opened, the capillary was exposed to this atmosphere so that water loss due to evaporation was negligible. The water column height was found to be stable over a long period of time. Each run of the experiment began by having the valve closed and using the syringe to set the initial column height. The valve to the buffering cup was then opened to let the meniscus rise or fall in a self-organized manner.

The meniscus was illuminated with a fiber optic light source positioned below the beaker because we found that the best intensity contrast between the meniscus and the background was achieved when the light came directly from below. The use of the optical fibers put the lamp far away from the system and minimized the disturbance of a heat source. To observe the pinning dynamics, an inspection microscope was mounted horizontally and coupled to a charge-coupled device (CCD) camera. The position of the microscope was adjusted such that the center of the image field

coincided with the equilibrium height. This enabled us to perform rise and fall experiments without repositioning. The vertical field captured by the camera was 3.5 mm over 640 pixels, which corresponds to a resolution of about 5.5 μm/pixel. At set time intervals, the video image was digitized and processed by a microcomputer to determine the meniscus position. A typical gray-scale image is shown in Fig. 5(b). The intensity pattern results from the curved meniscus reflecting the light coming from below and passing through the cylindrical sidewall. This pattern remains essentially the same across the imaging field. By choosing a proper threshold, the gray-scale image was converted to a binary bitmap image for edge detection. Figure 5(c) shows the outline of the meniscus after image processing. After removing noise by image editing, the lower edge of the meniscus was identified and the pixel coordinates were used to compute the average position of the meniscus. This gives the relative height $h'(t)$ of the water column within the imaging field. The noise in the data came primarily from the resolution limit and intensity contrast of the image. We estimated that the uncertainty was about $\Delta h' = \pm 0.13$ pixel.

Data far from the pinning threshold were collected using a wide-angle (8-mm focal length) camera lens instead of the microscope. An image field of 14 cm was captured. The fast dynamics had to be recorded onto video tape and played back frame by frame for analyses. The absolute height of the meniscus above the beaker's water level (h) was observed visually on the video monitor. The accuracy ($\Delta h = \pm 0.8$ mm) was limited by several factors: the resolution of the video system, the distortions of the picture due to reflections in the capillary tube, and the contrast in the image. The time t was determined to an accuracy of about $\Delta t = \pm 10$ ms.

C. Temperature stability

Temperature stability is of critical importance in the experiment, especially in the pinning region. A slow change in temperature can result in a slow movement of the contact line that has nothing to do with pinning. The dominant effect comes from the temperature dependence of the surface tension γ, which directly affects the equilibrium height. Changes in the viscosity is unimportant because the flow is very slow. Differential thermal expansion of glass and water is a minor effect. As shown in Fig. 5, the main parts of the apparatus are enclosed in a temperature controlled and thermally insulated chamber. Figure 6(a) shows the column height data from a series of rise and fall experiments for a 300-μm-diam S tube taken without temperature control. The drifting ambient temperature was recorded and displayed in the same plot. We note that the temperature dropped almost linearly during the time of the experiment at an approximate rate of 2.2 mK per minute. The equilibrium height H_{eq} was found to rise in a similar fashion because γ increases with decreasing T. The dotted line between the rising and falling data indicates the rising trend of H_{eq}, the slope of which was about 0.13 pixel per minute. Dividing the two rates yields a ratio $\Delta H_{eq}/\Delta T \approx -57$ pixel/K. With our resolution of 5.5 μm/pixel, this corresponds to a change in the equilibrium height $\Delta H_{eq} \approx 310$ μm for a temperature change of $\Delta T \approx 1$ K. Since the equilibrium height for the 300 μm ID capillary is $H_{eq} \approx 10$ cm, the percentage change is $\Delta H_{eq}/(H_{eq}\Delta T)$
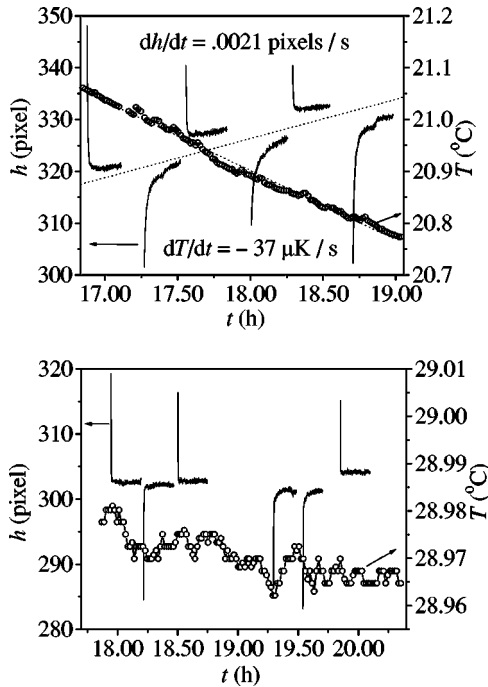
FIG. 6. If the temperature is not stable, consecutive capillary rise and fall runs would result in different final heights. This is mainly due to the fact that the surface tension of water changes with temperature by about 0.2%/K. (a) Without using temperature control, we find that a temperature rise of $\Delta T \approx 1$ K would cause a drop in the meniscus height by about 57 pixels (≈ 310 μm). (b) With temperature control, our setup was typically stable to within a few millidegrees over an hour and the menicus height did not change by more than a pixel. The data in both plots were taken with a 300-μm diam S tube.

$\approx 0.3\%$ K^{-1}. This is about the same as the thermal coefficient for the surface tension of water (-0.2% K^{-1}).

Figure 6(b) shows a typical set of data taken in the temperature controlled chamber. Over a period of 2 h the temperature variation remained within ± 10 mK. For a single rise and fall experiment that lasted about 15 min, the temperature was stable to within a few milli-Kelvin. The equilibrium height for several consecutive runs over this 2-h period showed no drift. In our later analyses of pinning, we used only runs for which $\Delta T < \pm 4$ mK. This corresponds to a change in equilibrium height of $\Delta H_{eq} \approx 1$ μm (≈ 0.2 pixel), about the same as the overall noise level. The temperature sensors we used were suspended freely in air. Since the apparatus has a much larger thermal mass than the sensors, it is safe to assume that the temperature variations of the water inside the tubes were less than what we recorded.

In addition to monitoring the temperature stability of the equilibrium height, we measured the temperature gradient along the length of the capillary tube. Three sensors were spaced evenly along the 30 cm length of the tube. A vertical temperature gradient of 23(1) mK/cm was observed. This corresponds to a change of $\Delta T \approx 0.2$ mK over the size of the pinning region (≈ 100 μm) we analyzed. Therefore, we can assume that the data were not affected by spatial and temporal temperature variation in any appreciable way.

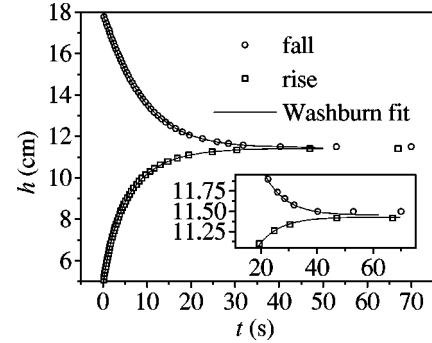FIG. 7. Low-resolution capillary rise and fall data for a 250-μm-diam S tube are well described by the Washburn equation. The fitting parameters are given in Table III and they agree well with theoretical values calculated by assuming a zero degree contact angle. The inset shows a magnified region near the equilibrium height. The difference between the final heights of rise and fall was barely detectable without the use of a microscope. The data were taken at 24.1 °C.

V. RESULTS AND ANALYSES

A. Washburn behavior versus critical behavior

Figure 7 shows the rise and fall $h(t)$ data taken with a 250-μm-diam S tube on a coarse scale. The solid lines are fits to Eq. (21), the Washburn equation. The two fitting parameters H_{eq} and τ_w were obtained both from the rise and fall data. They were also calculated from Eqs. (18) and (19) using the known experimental parameters and assuming $\theta = 0°$. Table III lists the three sets of results and they are in good agreement. Small differences can be attributed to the fact that θ may be nonzero or velocity dependent, and there may be small hystereses between advancing (rise) and receding (fall) experiments. In any event, there is no obvious evidence for pinning on the plotting scale that spans 13 cm. However, the magnified scale in the inset shows that there is actually a gap of about 1 mm between rise and fall after 50 seconds. This gap is actually relatively large among the many runs we made and it results from the fact that the tube was not used immediately after cleaning. The surface state was altered by simply exposing it to air. (The molecules adsorbed on the surface change with the environment and the rate of change depends on many factors such as temperature, pressure, and adsorption energy.) The gap was not readily visible only because the video resolution was limited to $\Delta h = \pm 0.8$ mm for the coarse scale data. With the higher resolution acheived by the microscope, we found that the contact line came to a complete stop. In contrast, Fig. 8(a) shows the high resolution data obtained in a 180-μm S tube immediately after it was cleaned. h' is the relative position within

TABLE III. Fitting results from the data displayed in Fig. 7 (250-μm ID S tube) and theoretical values for capillary rise using the Washburn equation ($\theta = 0°$).

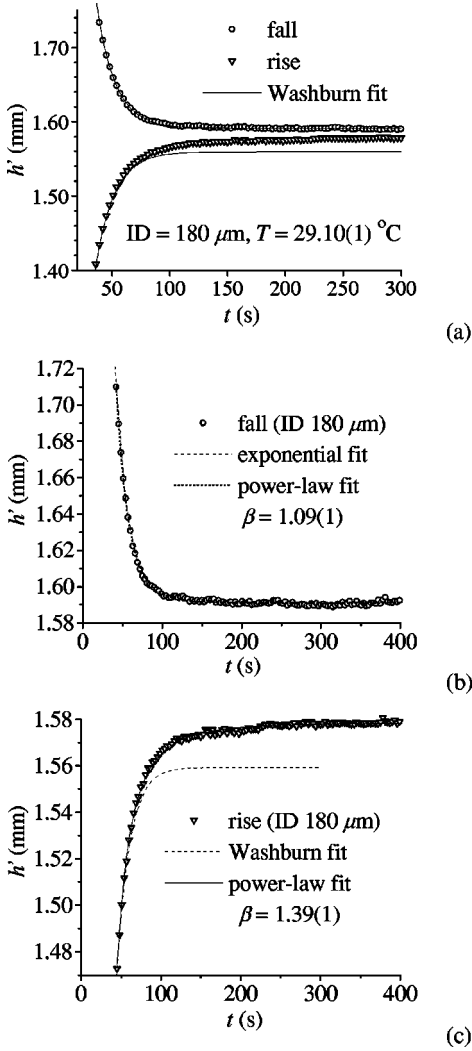|	H_{eq} (cm)	τ_w (sec)
Rise	11.43(1)	5.8(3)
Fall	11.45(1)	5.0(3)
Washburn	11.75	5.6

FIG. 8. (a) High-resolution capillary rise and fall data obtained with a 180-μm S tube are compared to the Washburn equation. Only the rise data show significant deviations at later times. The Washburn time constants obtained from the rise [17.8(3) s] and fall [17.1(3) s] data are only slightly larger than the calculated value (16.7 s). The experimental values are adjusted to $h_0 = 0$ at 20 °C. (b) The fall data at the highest spatial resolution are well described by an exponential function that corresponds to $\beta = 1$. Fitting the data to an algebraic form results in an exponent very close to unity (≈ 1.09). (c) The high-resolution rise data at late times are best described by a power law. The exponent $\beta = 1.39(1)$ in this example. The Washburn equation fits the early time data well but fails at later times.

the viewing frame (differs from h by a constant) and it shows a gap of about 15 μm. We note that the Washburn equation fits the falling data completely and τ_w agrees within 2% with both the value obtained from the coarse scale data and that calculated from Eq. (19). The final height H'_{eq} within the frame is reproducible within 0.5 pixel. The higher magnification in Fig. 8(b) shows no difference between the fits to the mean-field exponential approach and a power law with $\beta \approx 1$. Thus, the falling data show no evidence of pinning in the S tube and this lends confidence to the fact that the tubes were sufficiently clean. However, we note that the rising data in Fig. 8(c) do deviate from the Washburn fit significantly at late times. Fitting them to Eq. (25) gives $\beta = 1.39$, which
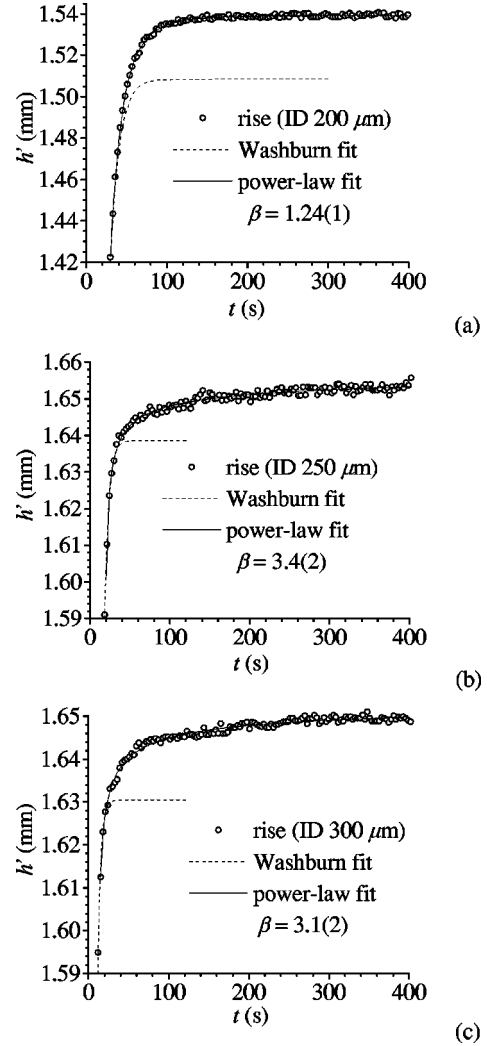
FIG. 9. High-resolution capillary rise data for S tubes with different ID's (200, 250, and 300 μm) all fit the power-law form and not the Washburn equation. However, the exponent β varies from case to case and there is no evidence of a universal value.

suggests that pinning effects are present. This contrast between the rise and fall data holds true for all the S tubes, but the values of β varies over a wide range: from 1.1 to 4. Figure 9 shows several fits of the rising data obtained with different tube diameters. Fits to the corresponding falling data are not shown because they are all similar to Fig. 8(a), well described by the Washburn equation in every case.

For the R tubes, the coarse scale data are similar to Fig. 7 and they fit the Washburn equation well. However, the high resolution data in the pinning region are different from Figs. 8 and 9. Figure 10 shows several sets of falling data obtained consecutively in a 250-μm-diam R tube. Each run lasted about 15 min and the starting times are indicated. They clearly show the stick-slip behavior assumed in the scaling theories. We did not attempt to determine the avalanche size distribution, in part because of inadequate resolution in measuring the size, but also because the events are correlated among different runs in the same tube. (It was unfeasible to study a large number of tubes.) We note, for example, every run in Fig. 10 shows sticking at $h' \approx 0.6$ mm. However, the time it took to overcome the pinning is random [54]. This implies that either the disorder is not completely quenched or
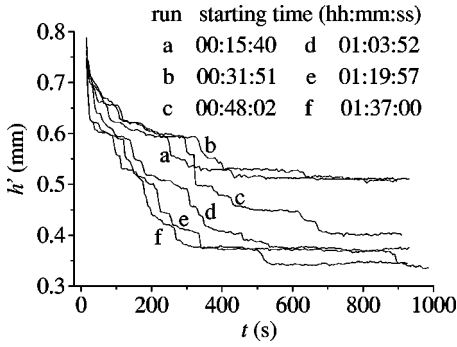
FIG. 10. High-resolution capillary-fall data from a 310-μm R tube show stick-slip behavior. Consecutive runs do not show exactly the same trace, but there are clearly strong pinning defects at certain positions, e.g., $h' \approx 0.6$ mm. That the amount of time it took to depin from these defects varied from run to run implies that either the disorder is not completely quenched, or that thermal/temporal noise play an important role.

the background temporal noise is important. The history of the system may also play a role because each rise and fall event can alter the adsorbed water molecules on the surface and they become part of the disorder for the next event. In addition, discrete movement of the entire meniscus suggests that the correlation length exceeds the system size ($\xi \sim r$), in which case fitting the data to Eq. (25) would be inappropriate. Such analyses are only valid when small parts of the contact line undergo discrete jumps while the average position of the line appears to change smoothly. In other words, the roughness in the R tubes is too large and the observed stick-slip behavior could be caused by finite-size effects. In the S tubes, the surface roughness is weak and the movement appeared to be continuous, but the disorder was shielded from the contact line by a wetting film during the fall experiment. Only in the rise experiments was the power-law behavior observed.

B. Waiting-time effect

To test the above explanation, we performed repetitive runs in S tubes by varying the waiting time (Δt) between successive rise experiments because the structure of the wetting film is expected to change during Δt and this would have an effect on the data. We varied Δt in the following manner. We first closed the valve leading to the water cap so that the pressure above the water column could be controlled by the syringe. In each run, the meniscus was first raised to the top of the image field to fully wet the interior wall. It was then lowered beyond the imaging field. After some time, we opened the valve and let the water column rise. Although the waiting position of the meniscus was not directly observed, we tried to keep it the same by displacing the same volume of air with the same flow rate that resulted in a meniscus velocity of about 1 mm/s. Δt is measured from the moment the meniscus passes H'_{eq} on its way down and the moment it reenters the frame on its way up. This is the total time available for the wetting film to reorganize. We found that the rise data were not reproducible. Figure 11 shows that the rise is generally slower with increased waiting time Δt, and this corresponds to a larger β. It is important to emphasize that Δt only affects the data near the pinning threshold and not
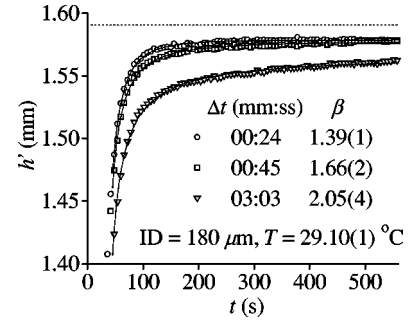

FIG. 11. Successive capillary rise experiments using a 180-μm S tube reveal that the waiting time Δt before the start of the rise affected the result. A longer waiting time resulted in slower rise and a larger exponent β. The horizontal dotted line indicates the final position of the falling column which can be taken as the equilibrium height. It was reproducible to within ± 3.5 μm.

the data far away. Fits of the early time rise data in different runs showed that the Washburn time constants τ_w was insensitive to the waiting time. The details of these fits were documented elsewhere [3]. Similar tests of waiting time effects were carried out for the falling experiments and we found that the data were reproducible to ± 0.5 pixel, within experimental tolerance. Fits to Eq. (25) always resulted in an exponent β consistent with unity. We also fitted the data to the exponential function of Eq. (26) that corresponds to $\beta = 1$. We found that the resulting parameters (H_c, τ_1) agreed with (H_{eq}, τ_w) obtained from Washburn fits of the coarse scale data. This result reinforced our conclusion that there was no detectable pinning effects in the falling experiments.

C. Empirical fits of the data

Since the analyses of the capillary rise data did not result in a unique value for β, one may question if Eq. (25) is the correct description and whether other empirical functions may fit the data better. To address this issue, we fitted the data to three different empirical functions:

$$h(t) = H_c - \frac{H_c - h_1}{1 + C \ln[1 + (t - t_1)/\tau_1]}, \qquad (27)$$

$$h(t) = H_c - \frac{H_c - h_1}{1 + [(t - t_1)/\tau_p]^p}, \qquad (28)$$

and

$$h(t) = H_c - (H_c - h_1) \exp\left[-\left(\frac{t - t_1}{\tau_s} \right)^s \right]. \qquad (29)$$

All three functions begin from the initial condition (h_1, t_1) and approach H_c as $t \to \infty$. The use of logarithm, power-law, and stretched exponential is intended to capture a wide range of dynamical behavior empirically. Each of these functions was also constructed to have three adjustable parameters just like Eq. (25) so that a fair comparison of the fitting errors can be made. For each data set over the same fitting range, fits to these functions were performed and the standard deviation δh of each fit was recorded. A fit of the same data to Eq. (25) was also carried out to obtain a standard deviation δh_β.
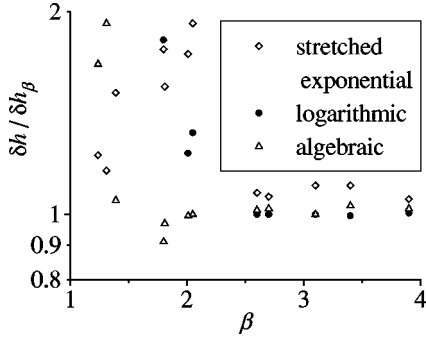
FIG. 12. Fitting the data to several empirical functions usually give errors that are larger than the power-law fits. The standard deviation of the empirical fits (δh) are normalized by the corresponding one for the power-law fit (δh_β). Overall, the power-law describes the data best, though the runs with $\beta > 2.5$ are quite well described by other functions.

Figure 12 depicts the ratio $\delta h / \delta h_\beta$ for various data sets that correspond to β between 1 and 4. We note that for data sets that correspond to $\beta > 2.5$, all three empirical functions fit the data about equally well as Eq. (25). However, for the data sets that correspond to $\beta < 2.5$, they give larger errors than Eq. (25). Only the algebraic function matches Eq. (25) on some data sets. The other two functions give δh up to four times as large as δh_β. Thus Eq. (25) gives the best description of the data overall, but the algebraic function in Eq. (28) works almost as well.

The standard deviations δh_β of the fits to Eq. (25) are depicted in Fig. 13(a). We find that they are on the order of the intrinsic noise and resolution of our apparatus ($\Delta h' = \pm 0.13$ pixel) and there are no correlations with the tube
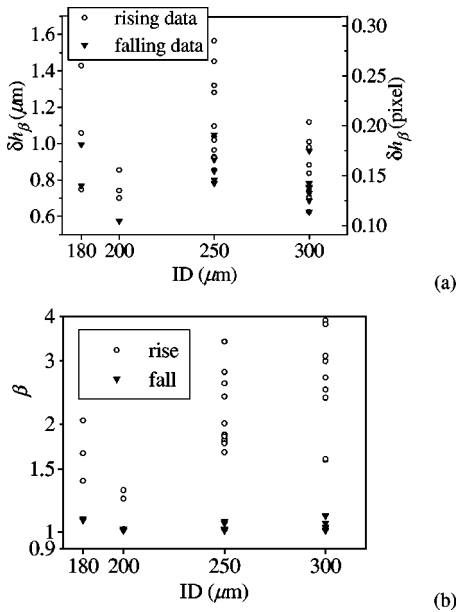

FIG. 13. (a) Standard deviations of the power-law fits, δh_β, are plotted against the ID's of the tubes. Each point represents a separate run. That δh_β is less than 1 pixel shows that the fits work very well. (b) The exponent β obtained for different tubes versus the ID's. Note that all capillary fall runs give β close to unity, but the rise experiments have β between 1 and 4 regardless of the tube diameter.
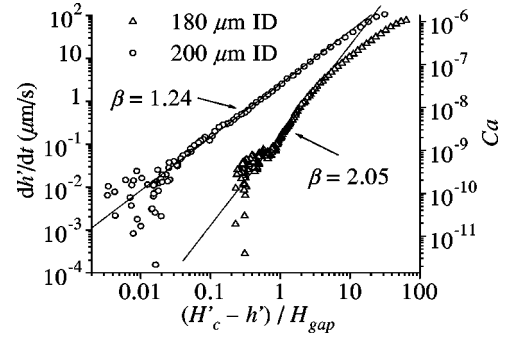

FIG. 14. Interface velocity $v = dh'/dt$ (or capillary number Ca) are plotted against the reduced driving force $f = (H'_c - h')/H_{gap}$ on log-log scales for a 180- and a 200-μm S tube. Note that the power-law behavior of Eq. (1) was typically observed for $f < 4$, but the exponent β, as given by the slope of the plot, is nonuniversal.

diameter. For the falling data, the values of δh_β are usually slightly smaller than those for the rising data. This may be due to the fact that the disorder is shielded by the wetting film and there is less intrinsic noise in the dynamics. Figure 13(b) shows the exponents β obtained for the various tube sizes. We note that β is always larger than unity, ranging between 1 and 4. The values show no systematic trend with the tube radii, but there is a clear difference between rising and falling columns. For the falling experiments, β is always close to unity, but for the rising experiments β varies widely. It is safe to say that we did not observe universal behavior.

D. Strength of disorder

In addition to the actual values of the exponent β, it is also important to know how the strength of disorder affects the size of the critical region and other parameters in the fits. For example, if the fits were not purely empirical, one would expect the critical region to scale with the strength of the disorder in the system. Since the falling experiments give the equilibrium height H_{eq} for every tube and the pinning height H_c is known from the rising experiment, $H_{gap} \equiv H_{eq} - H_c$ is a natural measure of the disorder for every tube. To identify the critical region, we show in Fig. 14 plots of the velocity $v = dh'/dt$ versus the reduced driving force $f \equiv (H'_c - h')/H_{gap}$ for two different cases. The two data sets are replots of the original h versus t data shown in Figs. 9 and 11. The fits to Eq. (25), not Eq. (24), are represented by straight lines on the log-log scales. It can be seen that the noise in the velocity data is much worse than the h versus t data because of numerical differentiation, and the problem is most severe in the low velocity limit. Data points at high velocity not used in the original fits are included to show the departure from power-law behavior. We observe that the power-law fits in Figs. 9 and 11 hold over two to three decades in the velocity v (or Ca), which is as good or better than previous studies. When β is close to unity (1.24), the data span a similar range in f. For larger $\beta (= 2.05)$, the range in f is necessarily reduced because the velocity data reach the noise floor at small f values. We should note that both fits have an upper limit near $f \approx 4$ and $Ca \approx 10^{-7}$. They also have about the same lower limit in the velocity ($Ca < 10^{-9}$), which is smaller than most previous experiments. Although only two cases are shown here, we found similar
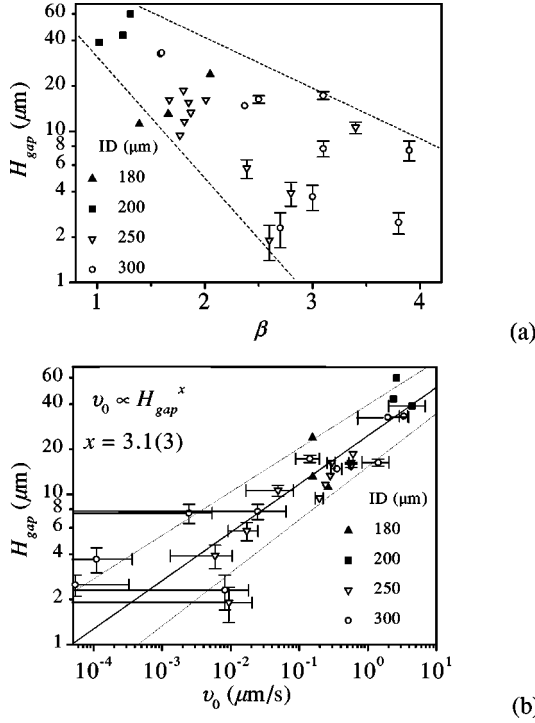
FIG. 15. H_{gap} is a measure of the disorder strength. (a) and (b) show the empirical correlations between H_{gap} and the two parameters β and v_0 in Eq. (1). Each point in the plot is obtained from a pair of consecutive rise and fall runs. There is less scattering in (b) and it suggests a proportionality $v_0 \propto H_{gap}^3$.

FIG. 16. Following Eqs. (32) and (33), H_{gap} and v_0 are rescaled to remove their intrinsic r dependence. However, plots of $\tilde{H}_{gap}$ versus β in (a) and $\tilde{H}_{gap}$ versus $\tilde{v}_0$ in (b) do not show less scattering as compared to Fig. 15. We attribute the scattering to unknown microscopic changes on the surface.

critical regions in all the fits. This suggests that there are some underlying physical reasons for the form of Eq. (24) despite the fact that there appears to be no universality in the exponent β.

In our analyses, we also explored if the strength of disorder affected either the exponent β or the amplitude v_0 in Eq. (24). Figure 15 shows how H_{gap} is correlated with these two parameters. We observe that β is generally smaller for larger values of H_{gap}. This could be explained by the fact that stronger disorder would cause the movement to come to a more abrupt stop and, according to the behavior depicted in Fig. 3, that corresponds to a smaller exponent. In contrast, the data shows that the amplitude v_0 increases strongly with H_{gap}. An empirical fit to the form $v_0 \propto H_{gap}^x$ results in a large exponent $x = 3.1(3)$. The cause of this behavior is unclear. Although one would expect stronger disorder to cause the velocity to deviate from the Washburn behavior more readily, this effect is already accounted for in Eq. (24) by using H_{gap} to scale the driving force. The real reason is perhaps that because all the fits to Eq. (24) have about the same upper limits for v and f, smaller exponents must correlate with larger amplitudes. A plot of v_0 versus β confirmed such a correlation and it exhibits about the same level of scattering as Fig. 15(a).

Figure 15 may not be a fair representation of the effects of disorder because H_{gap} is clearly dependent on the tube radius r and we have not corrected for this intrinsic r dependence. Physically H_{gap} must go to zero as $r \to \infty$. To compare the strength of the disorder in different tubes, we should find the r dependence and normalize H_{gap} accordingly. We note that, assuming uncorrelated disorder, the threshold pin-
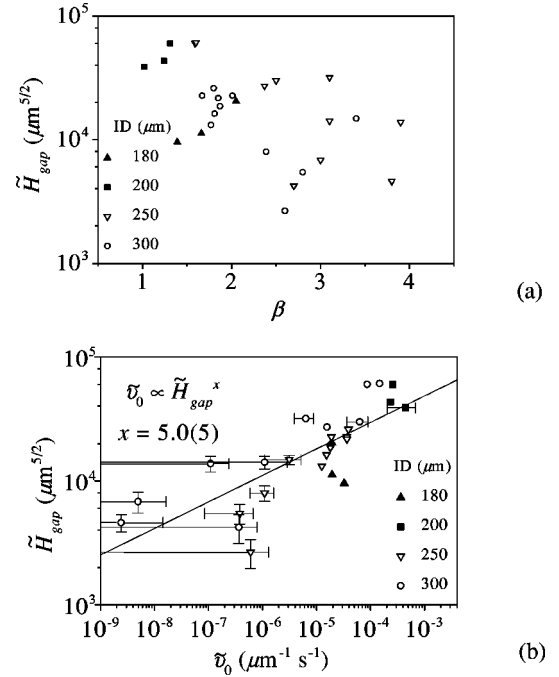
ning force F_c is proportional to the square root of the number of defects encountered by the contact line. Since the length of the contact line is $2\pi r$, we expect $F_c \propto \sqrt{r}$. The actual value of this force is given by $\pi r^2 \rho g H_{gap}$. Thus we can write

$$\pi r^2 \rho g H_{gap} = F_c \propto \sqrt{r}, \tag{30}$$

which gives

$$H_{gap} \propto r^{-3/2}, \tag{31}$$

consistent with the expectation that $H_{gap} \to 0$ as $r \to \infty$. A normalized measure of disorder for different tube radii may be given by

$$\tilde{H}_{gap} \equiv (H_{gap} r^{3/2}). \tag{32}$$

Similarly, based on Eqs. (18) and (19), we expect the velocity in different tubes to have an intrinsic r dependence given by $H_{eq}/\tau_w \propto r^2$. Thus it is appropriate to define a rescaled velocity

$$\tilde{v}_0 \equiv v_0/r^2 \tag{33}$$

for different tube radii Figs. 16(a) and 16(b) show plots of $\tilde{H}_{gap}$ versus β and $\tilde{v}_0$, respectively. They show qualitatively the same correlations seen in Fig. 15 with about the same level of scattering. A fit of the data in Fig. 16(b) to the form $\tilde{v}_0 \propto \tilde{H}_{gap}^x$ results in $x = 5$. This may be purely empirical considering the scattering of the data points.

Taken together, these results show that Eq. (24) describes the data very well. The fitting parameters show reasonable

correlations with the strength of disorder, but there is no evidence of a universal scaling exponent. The waiting time dependence suggests that the wetting film on the surface plays a crucial role in the pinning dynamics. Clearly, when the film has more time to reorganize, wet or dewet, it would alter the exposure of the surface roughness. Whether the physical changes are discrete molecular movements or continuous hydrodynamic flow (spreading or draining) is beyond our detection in this experiment.

VI. NUMERICAL SIMULATION

A. A one-dimensional model for the R tubes

The analyses in the preceding section cannot be applied to the rough (R) tubes because the stronger disorder caused the contact line to execute discrete jumps near the pinning threshold. To better understand this behavior, we carried out a numerical simulation to compare with the data. We note that the stick-slip behavior seen in Fig. 10 results from the fact that the sizes of the avalanches are not much smaller than the total length of the contact line, i.e., it is a kind of finite-size effect. In the extreme limit, the entire contact line executes discrete jumps and the system becomes effectively one dimensional. By studying a 1D model with quenched disorder, we can determine if the experiment was actually in that limit and what effects are important in the real systems. In addition, we can investigate the effects of the defect strength and spatial correlations which we cannot easily control in the experiment. Our starting point is a generalized version Eq. (16),

$$\frac{d}{dt}\left[\rho\pi r^2(h+h_0)\frac{dh}{dt}\right]=2\pi r\gamma\cos\theta-\pi r^2\rho gh$$

$$-8\pi\eta(h+h_0)\frac{dh}{dt}+F_d(h),$$

(34)

which is just a direct application of Newton's second law. The left-hand side is the rate of momentum change of the fluid column. The details of the flow field near the inlet and the meniscus are ignored. (See Ref. [3] for a discussion of this approximation.) The relevant forces are on the right-hand side: $F_d(h)$ represents the quenched random pinning forces distributed along the direction of motion. Using the normalized time and height variables (x,y) defined for Eq. (21), the equation can be expressed in a dimensionless form:

$$\frac{1}{a}\frac{d}{dx}\left[y\frac{dy}{dx}\right]=(1-y)-y\frac{dy}{dx}+F(y),$$

(35)

where $a=8\tau_w\eta/r^2\rho$, and $F(y)=F_d(h)/[\pi r^2\rho g(H_{eq}+h_0)]$ is the defect force normalized by the weight of the equilibrium water column. By assuming different amplitudes and spatial correlations for $F(y)$, we can integrate the equation numerically to see how $y(x)$ compares to the experimental rise and fall data. The techniques of integration are standard [55] and they are described in details in Ref. [3].
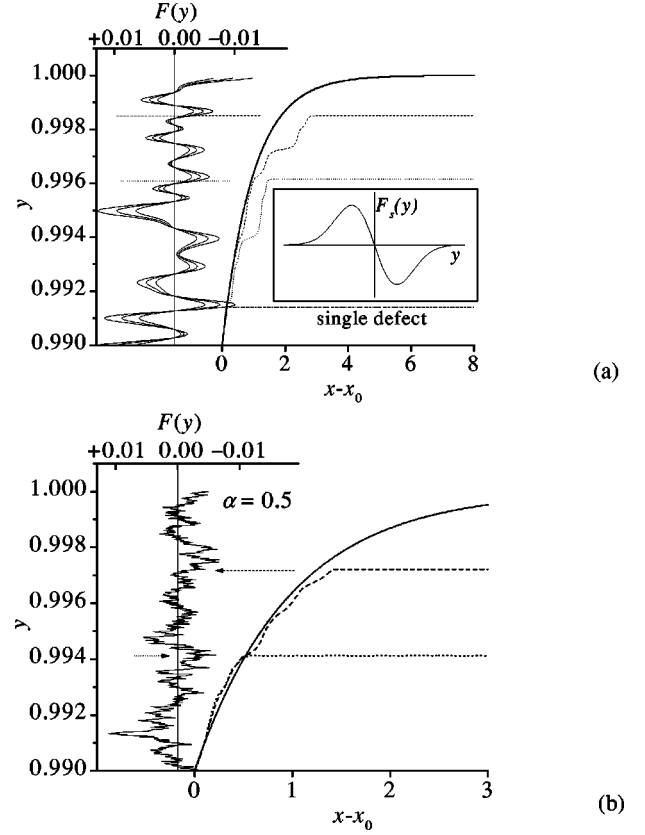

FIG. 17. Examples of simulated capillary rise data using the one-dimensional model represented by Eq. (35). The random pinning force $F(y)$ in (a) is generated by superposition of 300 randomly placed defects, each having the same strength and the same form shown in the inset. $F(y)$ in (b) has power-law correlations that correspond to self-affine surface roughness. In each plot, we show three simulated rise curves that correspond to three different amplitudes in $F(y)$.

B. Results

The first type of defects we studied are uncorrelated pits and bumps on the surface [see Fig. 4(e)]. The pinning force due to a single pit is depicted in the inset of Fig. 17(a). It has the general feature of having a positive maximum followed by a negative minimum as y increases. This shape was suggested by Raphaël and de Gennes [38]. For simplicity, we used the derivative of a Gaussian. The change in sign in F with increasing y means that a rising contact line would speed up on approaching the pit and slow down after passing the deepest point. A falling contact line would do the same with decreasing y. A bump on the surface can be represented by reversing the sign of F in the inset of Fig. 17(a): the contact line would first deccelerate and then accelerate upon passing through it. The traces on the left half of Fig. 17(a) represent the same force profile $F(y)$ with three different pinning strengths and those on the right half of the figure are the corresponding simulated capillary rise data. The standard Washburn behavior is included as reference and represented by the smooth solid line. The force profile was obtained by placing 300 pits randomly in the last 1% of the rise below the equilibrium height. For simplicity, the size and strength of all the pits were kept the same. The distance between the maximum and minimum of $F(y)$ was set at 5×10^{-4} (or 5%

of the region of investigation). The pinning strength was varied by changing the maximum force (F_{max}) of the single defect. The three cases in the figure have $F_{max}=6\times10^{-4}$, 9 $\times10^{-4}$, and 12×10^{-4}. (By definition, $F=1$ corresponds to the weight of the equilibrium fluid column inside the tube and it has a length of $H_{eq}+h_0$.) As one would expect, with increasing F_{max}, the contact line stops at a lower position. This pinned position is always slightly below a negative peak in $F(y)$, i.e., the contact line stops when it encounters a local maximum in the (downward) pinning force and does not have enough momentum to go over the barrier. Before reaching the final position, the contact line barely passes over several barriers and its velocity would come close to zero each time. Thus the $y(x)$ data resemble the experiment data in Fig. 10. That the repetitively runs in the real experiment ended in different final positions may be explained by the fact that there were changes in the wetting film thickness and they modified the overall strength of the pinning force. However, an important difference from the 3D real system is that, while the velocity speeds up and slows down in the simulation, there are no genuine singularities or true stick-slip events. In other words, even when the real contact line is limited by finite-size effects, it still has an infinite number of different configurations. If a part of the line is pinned by a strong defect, other parts can slowly rearrange themselves. When the elastic energy stored in the deformed line becomes larger than the potential barrier of the strong defect, it can result in a jump over the defect. This is the essence of avalanches and it cannot be represented by the 1D model. Another important feature of Fig. 10 is that the amount of time the contact line takes to depin from a strong defect varies from run to run. In contrast, the simulated behavior is deterministic. This can be attributed to the fact that there are always background temporal noise and vibrations in the real system that can help sections of the contact line get over small barriers. This effect is also absent in the model.

To contrast with the uncorrelated pits model discussed above, we studied the effect of defect forces with algebraic spatial correlations. The force-force correlation is *assumed* to be given by

$$G(r)\equiv\langle[F(y)-\bar{F}][F(y+r)-\bar{F}]\rangle_y\propto r^{2\alpha},\qquad(36)$$

where $\bar{F}$ is the average force, r is a spatial distance over which the correlation is calculated, and $\langle\ \rangle_y$ denotes an average over all possible choices of y. The left half of Fig. 17(b) shows an example of a defect force profile $F(y)$ over a 1% distance below the equilibrium height. It was generated with $\alpha=1/2$ and the (fractal) Hausdorff dimension of the profile is given by [56]

$$D_H=2-\alpha=3/2.\qquad(37)$$

This kind of force profiles may be applicable to surfaces with correlated chemical defects or geometric roughness, but there is no first-principle proof of how these surface properties affect the exponent α. The algebraic form of the force correlation is intuitively reasonable and offers a comparison with the uncorrelated model above. The technique for generating the profile is described in Ref. [3]. We note here only that both the rms force fluctuations A and the fractal dimen-
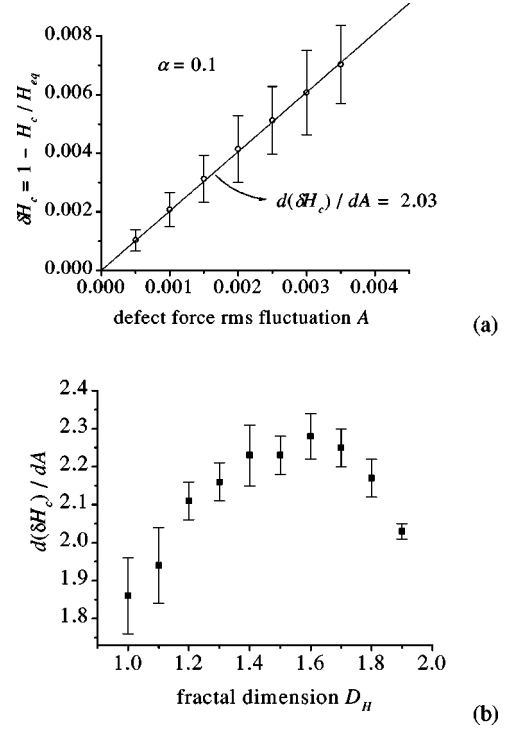

FIG. 18. In the 1D simulation of capillary rise with spatially correlated pinning force, the pinned height H_c depends on both the exponent α ($=2-D_H$) defined in Eq. (36) and the rms force A. (a) shows that H_c decreases linearly with A for a given value of α. (b) shows that the sensitivity of H_c is strongest for α between 0.3 and 0.6, or D_H between 1.4 and 1.7.

sion D_H can be varied independently. The right half of Fig. 17(b) shows how the simulated $y(x)$ data (dotted line) compared with the referenced Washburn behavior (solid line). A third trace (dashed line) shows the simulated data for the same roughness profile with half the force strength. As in Fig. 17(a), the weaker pinning force results in a higher final position. In both cases, the eventual pinned position corresponds closely to a local maximum in the downward force. Unlike Fig. 17(a), however, there are no other well-defined sticking points where the velocity is nearly zero. The reason is that the defect force fluctuates randomly at a length scale equal to the resolution we carried out the integration and so the neighboring peaks and valleys in the $F(y)$ curve counteract the effects of each other. They cause the contact line velocity to fluctuate on the same length scale without coming near a complete stop until the line comes to its final position. To understand this effect better, we carried out the simulation with different values of the fractal dimensions D_H and rms force strength A to see how they affect the final pinned height H_c. For each D_H, 100 different force profiles were generated, and the rms force of each was varied between 0 and 0.004 in increments of 0.0005. Equation (35) was integrated for each case to determine the pinned heights and averaged over the 100 realizations. Figure 18(a) shows an example (with $\alpha=0.1$ or $D_H=1.9$) of how the pinning height H_c changes with increasing rms force A. The difference between H_c and the equilibrium height H_{eq} is expressed in terms of a dimensionless variable $\delta H_c=(H_{eq}-H_c)/H_{eq}$ and we found that δH_c increases linearly with A. The error bars in δH_c represent the standard deviations in the 100 re-

alizations. The slope $d(\delta H_c)/dA$ for different fractal dimension D_H are summarized in Fig. 18(b). It is interesting to note that the maximum slope occurs with intermediate values of D_H, or $\alpha \approx 1/2$.

VII. DISCUSSIONS AND CONCLUSIONS

A. Summary of experimental results

We have studied the dynamics of capillary rise and fall over a range of contact line velocity that spans approximately six decades: 10^{-2} μm/s$<v<10^4$ μm/s. This corresponds to capillary numbers over a range $10^{-10}<Ca<10^{-4}$. There are two regions of distinct behavior. For $Ca \gtrsim 10^{-7}$ we find that the results are well described by Washburn equation and the surface disorder is unimportant. For $Ca \lesssim 10^{-7}$, there is much evidence that the microscopic details near the contact line affect the macroscopic behavior considerably. Surface roughness is only one of many possible sources of influence though it has often been the focal point of theoretical discussions. There are many other factors that can play a role in real systems and it is difficult to isolate the effects of surface roughness to compare with the theories. Nevertheless, our results provide useful information and insights on contact line dynamics.

By using a microscope to visualize the meniscus near the pinning threshold, we were able to directly observe stick-slip behavior in those capillary tubes with rough interior walls. This lends support to the qualitative picture of dynamic phase transitions in systems with quenched disorder [11]. However, in the consecutive rise and fall runs, we found that the amount of time it took for the contact line to depin from the strong defects was random. This implies that either the disorder in the system was slowly changing, or that the thermal/temporal noise in the system played an important role. These two possibilities cannot be distinguished. The fact that we were able to resolve individual avalanches implies that the data were limited by the finite size of the system and they cannot be compared to the continuous behavior of Eq. (25). Unfortunately, we were unable to study the statistical behavior of the stick-slip dynamics in terms of the time and size distributions of the avalanches because it was impractical to study a large number of sample tubes with different disorder configurations. In order to determine the exponent β in Eq. (25), we could only use capillary tubes with much weaker disorder so that the individual avalanches were below our experimental resolution and the length of the contact offers sufficient statistical averaging. The S tubes we used appear to meet these criteria and they gave results that were distinctly different from the R tubes.

In fitting the S tube results to Eq. (25), we found that the falling data always gave $\beta \approx 1$. Since the exponential function in Eq. (26) also corresponds to $\beta=1$, we fitted the falling data to the exponential form. We found that the time constant was always consistent with the Washburn value τ_w, which could be determined independently by either fitting data far from the pinning threshold or by direct calculation using Eqs. (18) and (19) with the known experimental parameters. The final height within the image field (H'_{eq}) was found to be reproducible to within ± 3.5 μm upon repeated falling runs in the same tube. The variation results from changes in the surface tension due to small instabilities in the

temperature. By applying a small offset to the data to compensate for the change in surface tension, the data from different runs all fell onto a single curve. We can therefore safely conclude that our falling experiments with the S tubes were free of pinning effects within experimental resolution. The same cannot be said about the capillary rise experiments.

For the rising data in the S tubes, we found that fits to Eq. (25) always gave $\beta>1$ and the result varies from run to run. The final height of each run always came within a few microns of the falling data [see Fig. 8(a)]. It implies that the disorder experienced by the rising contact line was extremely weak, yet the effects are clear because the Washburn equation and the exponential function do not fit the data near the pinning threshold. The algebraic form of Eq. (25) fits the data the best, but the exponent β varies between 1 and 4, clearly inconsistent with the RG prediction of $\beta \approx 2/3$ [15]. The larger observed exponent implies slower dynamics. One possible explanation is that the theory does not take into account the fact that the fluid volume is a conserved quantity and the movement of the contact line requires a finite amount of time to transport the fluid according to the appropriate hydrodynamic equations. Instead, the theory only considered the energetics associated with the interfaces joint at the contact line. This is analogous to treating domain-wall dynamics in a magnetic system in which a cluster of spins can all flip instantaneously to cause an avalanche. That the dynamics in such systems with nonconserved order parameters is faster than those with conserved order parameter is well established in the study of equilibrium phase transitions [57]. We expect the same to hold for dynamical phase transitions but this is not a solved problem. We should also emphasize that even if such theoretical analyses exist, they would not explain why repeated runs could give different values of β. Clearly, other (nonuniversal) effects specific to the system have to be considered.

B. Effects of viscous dissipation

The first effect to consider is viscous dissipation associated with the breakdown of the no-slip boundary condition near the contact line. We note that the derivation of Eq. (25) is based on the assumption that the contact angle is independent of velocity, which is unphysical. A more correct treatment of capillary rise should include a velocity-dependent dynamic contact angle in Eq. (16) and analyze the asymptotic behavior in the low velocity limit. The usual relationship used for the dynamic contact angle is (see e.g., [31])

$$\cos \theta_d = \cos \theta_a - ACa^B - D\left(\ln \frac{L}{l_s}\right)Ca, \qquad (38)$$

where θ_a is the static advancing contact angle. This equation is a modification of Eq. (8) with an added term linear in Ca. It arises from the intrinsic viscous stress which is always more important at higher velocities. L is a macroscopic cutoff length related to the system size and l_s is the microscopic slipping length of the order of 10 Å. D (≈ 5) is a dimensionless constant. The nonlinear term on the right-hand side of Eq. (38) is more important in the low velocity limit
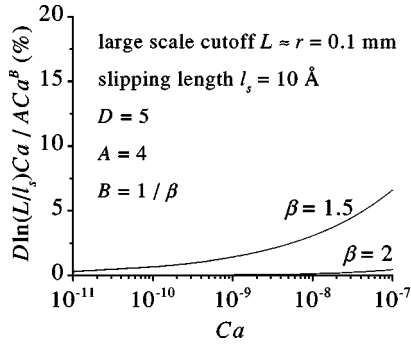
FIG. 19. A plot of the ratio of the linear to the nonlinear term in Eq. (41) for $\beta=1.5$ and $\beta=2$ shows that, even for β not much larger than unity, the linear term in Ca contributes less than 5% for $Ca<10^{-7}$.

because the exponent $B=1/\beta<1$ in our system. Substituting θ_d for θ in Eq. (16) and dividing the entire equation by $2\pi r\gamma$ yields

$$\frac{4}{r}(h+h_0)Ca=\cos\theta_a-ACa^B-D\left(\ln\frac{L}{l_s}\right)Ca-\frac{\rho gr}{2\gamma}h. \tag{39}$$

Solving for $h+h_0$ gives

$$h+h_0=\frac{1}{(4Ca/r)+(\rho gr/2\gamma)}$$
$$\times\left[\cos\theta_a-ACa^B-D\left(\ln\frac{L}{l_s}\right)Ca+\frac{\rho gr}{2\gamma}h_0\right]. \tag{40}$$

For low capillary numbers and under typical experimental conditions ($Ca\lesssim10^{-7}$, $r\approx0.1$ mm), the ratio of the two terms in the denominator is $(4Ca/r)/(\rho gr/2\gamma)<0.06\%$. Hence we can ignore the Ca-term in the denominator of Eq. (40) and simplify it to

$$h=\frac{2\gamma}{\rho gr}\left[\cos\theta_a-ACa^B-D\left(\ln\frac{L}{l_s}\right)Ca\right]. \tag{41}$$

The relative importance of the linear and nonlinear terms in Ca is illustrated Fig. 19, where we plot their ratio as a function of Ca over a range that covers the pinning region in our experiment ($10^{-11}<Ca<10^{-7}$). The numerical values used in calculating the ratio are given in the figure and they are typical of the experimental parameters reported in the literature [49,31,41,47,52]. We calculated the ratio for two values of β. Even for β not much larger than unity, the linear Ca-term contributes no more than 5% at the highest velocity. Using Eq. (41) to fit some of our data confirmed that the viscous dissipation represented by this term is unimportant [3]. Thus, to a good approximation, the linear term can be ignored, and Eq. (41) is reduced back to Eq. (24). This rules out the possibility that our data were affected by viscous effects and justifies our use of Eq. (25) for analyses.

C. Effects of controlled velocity versus controlled force

A more important point to consider is whether the contact line is driven by a constant force or driven at a constant velocity, a subtle distinction emphasized by Raphaël and de-Gennes [38]. With an imposed velocity, the contact line would sweep across all surface defects no matter how strong they are, because the elastic energy due to the surface tension would always exceed any pinning barrier when the *average* position of the line is moved far beyond the defect. The power-law behavior of Eq. (24) results from averaging over the fluctuating force on the line, which is always *nonzero*. The situation is different in a real experiment such as ours where the applied force is given (though not necessarily held constant) and the velocity is allowed to fluctuate. For certain realizations of the surface disorder, the contact line may move at a velocity much less than the *average* velocity that corresponds to the given applied force F, including $v=0$. This is because the threshold pinning force F_c represents an average over all realizations for an infinite system; it is not the property of any single realization. A real contact line is of finite length and it does not sample all possible realizations of the disorder of a given strength in a single sample tube. Every experimental realization eventually stops in a $v=0$ state, but the residual force F is likely to be still above the average pinning force F_c, because once the line stops, it can no longer explore other configurations.

The problems associated with a controlled-force experiment can be viewed in different ways. First, we note that the theoretical velocity v is given by the statistical average $\langle dh/dt\rangle$. In the experiment, the travel distance Δh is set by the image field and the real measurement is on the travel time Δt, which varies from run to run. Thus the measured velocity reflects $\Delta h/\langle\Delta t\rangle$ while the theoretical velocity actually corresponds to $\Delta h\cdot\langle1/\Delta t\rangle$. In general, we expect $1/\langle\Delta t\rangle\neq\langle1/\Delta t\rangle$. In a constant-velocity experiment, this distinction is unimportant because the system spends equal time in each configuration. In a controlled-force experiment, the system spends more time in the deeper metastable states and the inequality holds. Hence the disagreement between theory and experiment is actually not surprising. This problem is compounded by the fact that real contact lines are of finite length and real experiments do not sample all possible realizations of the disorder or all possible line configurations. To appreciate these effects, we can consider how the ideal behavior depicted in Fig. 1 would be affected. The proposed physical picture near the critical point is that sections of the contact line would be pinned for a long time and depin via avalanches triggered by small movements in other sections. For a finite-size system, the metastable section can be the entire line, hence a slowly moving state ($v\approx0$) for the infinite system can become a truly pinned state ($v=0$) for a finite-size system. Even for an infinitely long line, inadequate statistical sampling implies that the threshold force F_c is ill defined, because F_c is defined theoretically as an average value for all realizations of the disorder. An experiment performed with a single tube can in fact reach a pinned state when the driving force F is still above this theoretical threshold F_c. A constant-velocity experiment, by definition, does not sample any of the $v=0$ states, but a controlled-force system can be trapped in one indefinitely. In other words, the
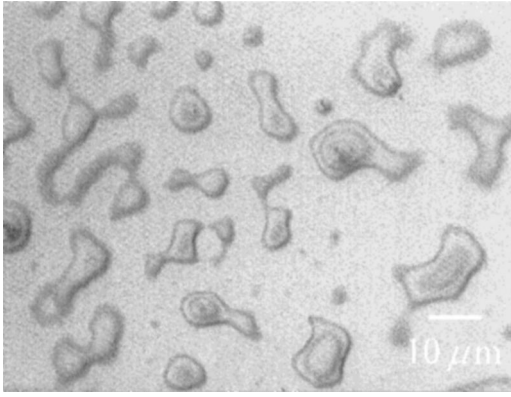
FIG. 20. After a large water drop passes over an uncleaned glass slide, many micron-size droplets remain stuck on the surface and they can be seen readily under an optical microscope. The existence of these droplets implies that there are strong deformations in real moving contact lines that are excluded from the theories. These fluctuations are more important in constant-velocity systems than in controlled-force systems.

$v=0$ states have no effects on constant-velocity systems but they have the strongest effects in controlled-force experiments, because the difference between $1/\langle \Delta t \rangle$ and $\langle 1/\Delta t \rangle$ is accentuated by these pinned states.

Another important factor to consider is the role of *strong deformations* in the line shape. Theories in the spirit of Eq. (9) assume weak deformation in the sense that the line shape is represented by a single-valued function. The possibilities that strong surface defects may cause overhangs or complete ruptures are excluded. Figure 20 illustrates a common phenomenon: when a drop of water passes over a dirty glass surface, smaller droplets are left behind. This is the result of strong pinning defects that cause a moving contact line to first form overhangs and then break off. These strong fluctuations occur when the velocity is held constant and the applied force is allowed to fluctuate with no upper bound. In a controlled-force experiment, these fluctuations are suppressed because they are separated from the weakly fluctuating modes by large energy barriers. Near the pinning threshold, the net driving force is weak and the line would be stopped by the barriers instead of passing over them.

D. Concluding remarks

We argued above that there are intrinsic reasons for the experiment to disagree with the theories and, in fact, it is not unreasonable to find different behavior from run to run because the disorder may not be completely quenched and small background noise is unavoidable. There is much evidence that small changes in the system can lead to large differences in the result. Theoretical predictions summarized in Table I actually support this conclusion. We note that most of the mean-field theories predict pinning exponents β in the range of $1/2 \leq \beta \leq 2$. The capillary-wave excitation mechanism proposed by Sheng and Zhou [31] predicts $2 < \beta < \infty$, with the exact value depending on the smoothness of the edge of the surface defects. These theories all contain some microscopic details, such as the wettability of the surface, the character of the heterogeneities in the system, the mechanism by which the contact line advances, and the

range of capillary numbers considered. Clearly, the details matter. Although we did not observe $\beta < 1$ as predicted by the renormalization-group analyses, that possibility is not completely excluded, because we did not analyze runs that have H_{gap} larger than several hundreds of microns. In those runs, the rise stopped abruptly, which is not inconsistent with the $\beta < 1$ behavior depicted in Fig. 3. However, since the $h(t)$ data up to the pinned position are well described by the Washburn equation, we cannot distinguish whether the line is pinned by a single strong defect or if there is actually a small critical region which we could not resolve. The main point we want to emphasize here is that the variability in our experimental results for β is consistent with the fact that the theoretical value also varies widely with the details of the models, even though they all result in the same power-law form.

The variability or irreproducibility of our experimental results should be distinguished from the findings of other earlier experiments as summarized in Table II. There are many factors that could have affected the previous experiments but not ours. First, we have shown that the measurements were sensitive to small changes in the temperature due to thermal effects on the surface tension. Durian *et al.* [58] have also noted that, in their capillary rise experiments using binary liquid mixtures, the thickness of the wetting layer changes with T and it can affect the results. As a result, we only analyzed data from runs with $\Delta T < \pm 4$ mK. In contrast, many previous experiments were performed at room temperature with much less stability. For example, Mumley *et al.* [36] stated a temperature stability of 21 ± 2 °C. Second, we have used deionized water as both the cleaning and the measuring liquid to minimize chemical complications. Many studies used immiscible liquids or liquid mixtures for which the surface chemistry is either complicated or unknown. The protocols for cleaning the surface undoubtedly varied as well, and they may have etched the surface or left behind foreign molecules. These factors are probably responsible for the very weak surface disorder in our system such that our experiment had to be performed down to a much lower range of capillary numbers. Since physical mechanisms operative at a different range of Ca could be quite different, our results may not be directly compared to many earlier studies. That Eq. (1) was uniformly adopted to fit the data could be accidental. We note, for example, Stokes *et al.* [49] observed a static advancing contact angle of 65° and a receding angle of 45°. This large difference implies that their system had much stronger disorder than ours and their measurements were made at capillary numbers several orders of magnitude higher. There is no *a priori* reason to believe that the same mechanisms are operative in the two studies and that the results should agree. A related issue is that most experiments did not clearly identify the critical region or established a mean-field region with different behavior. In contrast, we have shown that the mean-field Washburn equation describe the falling data completely and worked well for the rising data to within 100 μm from the pinned height. In Sec. V D, we noted that Fig. 14 and other similar plots of our data consistently found that the upper limit of power-law behavior occurs at a reduced driving force $f \approx 4$. The power-law form of Eq. (1) is typically obeyed over two decades in velocity, down to our noise level. Thus, despite the variability

in the exponent β, there is some consistency in the size of the critical region and it lends some confidence that Eq. (1) is not purely empirical.

Perhaps the most important findings in our experiment are that the dynamics of the capillary rise and fall are different near the pinning threshold and that the waiting time affects the rise dynamics. These are compelling evidence that the nature of the wetting film on the surface plays a crucial role in the macroscopic contact line dynamics. That a longer waiting time resulted in slower dynamics, a larger gap H_{gap} and a larger exponent β are intuitively reasonable as we expect the wetting film to become thinner with time and expose more surface defects. Similarly, that the receding contact line in the falling column showed no pinning effects can be explained by the fact that it always leaves behind a wetting film that shields the surface defects. It is interesting to note that, in a recent study, Salmeron *et al.* [59] used scanning probe microscopy to investigate water films adsorbed on mica surfaces. They found that the 2D structure of molecular layers changed with time at various humidity levels. Changes on the scale of a few microns were seen in a few minutes, presumably caused by thermal excitations. Although our experiments were performed in 100% relative humidity, we may expect similar thermal fluctuations in the film thickness over the same time scale. Thus the disorder in the system is not completely quenched. To the extent that we believe the wetting film plays a crucial role, it is then not surprising that the data varied from run to run even if there were no other changes in the system.

From a theoretical point of view, the fact that the wetting film affects the dynamics is a logical conclusion. As mentioned in Sec. II B, molecular-dynamics simulations have demonstrated that the conventional no-slip boundary condition in continuum hydrodynamics breaks down near the contact line. The stress singularity associated with the contact line is removed by introducing a *slipping length* $l_s \approx 10$ Å , which is comparable to an adsorbed wetting film. Clearly, in the presence of such a film, the liquid-vapor meniscus joins onto it smoothly and this would have an effect on the fluid motion. In particular, if the film thickness or its thermal fluctuations are comparable to or larger than l_s, the contact line becomes ill defined. Such molecular-scale details in the *slipping region* near the contact line would ultimately control the macroscopic dynamics. We should note that Durian *et al.* [58] have also independently concluded that microscopic changes of the wetting layer inside a capillary tube can have dramatic effects on the macroscopic behavior. To carry our reasoning one step further, we must conclude that *all* microscopic details near the contact line on the size scale of l_s are important, regardless of whether they are related to surface roughness, wetting films, or molecular interactions. This is because the slipping region becomes the bottleneck of contact line dynamics near the pinning threshold and the nature of this bottleneck determines how the water molecules would move through it.

Lastly, we should reemphasize that while the existence of avalanches has been confirmed, the prediction of universality in dynamical phase transitions was not borne out by our study. This may be no fault of the theory in the sense that, at or near the pinning threshold, the system is simply in a most delicate state which is infinitely sensitive to any perturbation. Real physical systems invariably have many perturbations that would cause the behavior to deviate from the scaling predictions. In approaching a dynamical transition, each small imperfection leads the system further down a path that departs from the ideal behavior and the effect is cumulative. This may be why the universality predictions have not been confirmed in *any* experimental system, yet the avalanche behavior is often observed. If the avalanche models could be generalized to incorporate the details of the transport mechanism and the effects of conservation laws, it will undoubtedly add to our understanding of the problem.

[1] E. W. Washburn, Phys. Rev. **17**, 273 (1921).

[2] E. Schäffer and P.-Z. Wong, Phys. Rev. Lett. **80**, 3069 (1998).

[3] E. Schäffer, Master's thesis, University of Massachusetts, Amherst, MA, 1997.

[4] S. Bhattacharya and M. J. Higgins, Phys. Rev. Lett. **70**, 2617 (1993).

[5] J. S. Urbach, R. C. Madison, and J. T. Markert, Phys. Rev. Lett. **75**, 276 (1995).

[6] J. S. Urbach, R. C. Madison, and J. T. Markert, Phys. Rev. Lett. **75**, 4694 (1995).

[7] M. C. Hellerqvist *et al.*, Phys. Rev. Lett. **76**, 4022 (1996).

[8] T. Delker, D. B. Pengra, and P.-Z. Wong, Phys. Rev. Lett. **76**, 2902 (1996).

[9] J. P. Stokes, A. P. Kushnick, and M. O. Robbins, Phys. Rev. Lett. **60**, 1386 (1988).

[10] J. Koplik and H. Levine, Phys. Rev. B **32**, 280 (1985).

[11] C. Tang and P. Bak, Phys. Rev. Lett. **60**, 2347 (1988).

[12] T. Nattermann *et al.*, J. Phys. (Paris) II **2**, 1483 (1992).

[13] O. Narayan and D. S. Fisher, Phys. Rev. B **48**, 7030 (1993).

[14] O. Narayan and D. S. Fisher, Phys. Rev. B **49**, 9469 (1994).

[15] D. Ertaş and M. Kardar, Phys. Rev. E **49**, R2532 (1994).

[16] A. W. Adamson, *Physical Chemistry of Surfaces*, 5th ed. (Wiley, New York, 1990).

[17] R. Wenzel, Ind. Eng. Chem. **28**, 988 (1936).

[18] A. B. D. Cassie and S. Baxter, Trans. Faraday Soc. **40**, 546 (1944).

[19] G. E. P. Elliott and A. C. Riddiford, Nature (London) **195**, 195 (1962).

[20] G. E. P. Elliott and A. C. Riddiford, J. Colloid Interface Sci. **23**, 389 (1967).

[21] A. Schwartz and S. B. Tejeda, J. Colloid Interface Sci. **38**, 359 (1972).

[22] T. D. Blake, *International Symposium on the Mechanics of Thin-Film Coating* (AIChE, New Orleans, LA, 1988).

[23] J. E. Seebergh and J. C. Berg, Chem. Eng. Sci. **47**, 4455 (1992).

[24] J. B. Cain, D. W. Francis, R. D. Ventor, and A. W. Neumann, J. Colloid Interface Sci. **94**, 123 (1983).

[25] R. S. Hansen and M. Miotto, J. Am. Chem. Soc. **79**, 1765 (1957).

[26] P. G. de Gennes, Rev. Mod. Phys. **57**, 827 (1985).

[27] C. Huh and L. E. Scriven, J. Colloid Interface Sci. **25**, 85 (1971).

[28] L. M. Hocking, J. Fluid Mech. **76**, 801 (1976).

[29] L. M. Hocking, J. Fluid Mech. **79**, 209 (1977).

[30] R. L. Hoffman, J. Colloid Interface Sci. **94**, 470 (1983).

[31] P. Sheng and M. Zhou, Phys. Rev. A **45**, 5694 (1992).

[32] J. Koplik, J. R. Banavar, and J. Willemsen, Phys. Rev. Lett. **60**, 1282 (1988).

[33] P. A. Thompson and M. O. Robbins, Phys. Rev. Lett. **63**, 766 (1989).

[34] J. W. May, in *Advances in Catalysis*, edited by D. D. Eley, H. Pines, and P. B. Weisz (Academic, New York, 1970), Vol. 21, p. 151.

[35] R. G. Cox, J. Fluid Mech. **168**, 169 (1986).

[36] T. E. Mumley, C. J. Radke, and M. C. Williams, J. Colloid Interface Sci. **109**, 398 (1986).

[37] K. H. Ishimi, Hikita, and M. N. Esmail, AIChE. J. **32**, 486 (1986).

[38] E. Raphaël and P. G. de Gennes, J. Chem. Phys. **90**, 7577 (1989).

[39] J. F. Joanny and M. O. Robbins, J. Chem. Phys. **92**, 3206 (1990).

[40] L. H. Tanner, J. Phys. D **12**, 1473 (1979).

[41] T. S. Jiang, S. G. Oh, and J. C. Slattery, J. Colloid Interface Sci. **69**, 74 (1979).

[42] R. L. Hoffman, J. Colloid Interface Sci. **50**, 228 (1975).

[43] E. Rillaerts and P. Joos, Chem. Eng. Sci. **35**, 883 (1980).

[44] B. S. Kennedy and R. Burley, J. Colloid Interface Sci. **62**, 48 (1977).

[45] E. B. Gutoff and C. E. Kendrick, AIChE. J. **28**, 549 (1982).

[46] T. E. Mumley, C. J. Radke, and M. C. Williams, J. Colloid Interface Sci. **109**, 413 (1986).

[47] M. Bracke, F. D. Voeght, and P. Joos, Prog. Colloid Polym. Sci. **79**, 142 (1989).

[48] G. Ström, M. Fredriksson, P. Stenius, and B. Radoev, J. Colloid Interface Sci. **134**, 107 (1990).

[49] J. P. Stokes, M. J. Higgins, A. P. Kushnick, S. Bhattacharya, and M. O. Robbins, Phys. Rev. Lett. **65**, 1885 (1990).

[50] P. Dimon, A. P. Kushnick, and J. P. Stokes, J. Phys. (Paris) **49**, 777 (1988).

[51] E. Charlaix and H. Gayvaller, J. Phys. (Paris) II **2**, 2025 (1992).

[52] S. Kumar, D. H. Reich, and M. O. Robbins, Phys. Rev. E **52**, R5776 (1995).

[53] T. Delker, Senior Honors Thesis, University of Massachussets, Amherst, MA, 1995.

[54] G. D. Nadkarni and S. Garoff, Langmuir **10**, 1618 (1994).

[55] W. H. Press, B. P. Flannery, S. A. Teukolsky, and W. T. Vetterling, *Numerical Recipes in C* (Cambridge Press, Cambridge, 1988).

[56] P.-z. Wong and A. J. Bray, Phys. Rev. Lett. **59**, 1057 (1987).

[57] P. C. Hohenberg and B. I. Halperin, Rev. Mod. Phys. **49**, 435 (1977).

[58] D. J. Durian, K. Abeysuriya, S. K. Watson, and C. Franck, Phys. Rev. A **42**, 4724 (1990).

[59] M. Salmeron, L. Xu, J. Hu, and Q. Dai, MRS Bull. **22** (8), 36 (1997).